

Article

Benchmarking L-PBF Systems for Die Production: Powder, Dimensional, Surface, Microstructural and Mechanical Characterisation

Jose Manuel Costa ^{1,2,*} , Elsa Wellenkamp Sequeiros ^{1,2} , Ruben Filipe Santos ^{1,2,3} 
and Manuel Fernando Vieira ^{1,2} 

- ¹ Department of Metallurgical and Materials Engineering, Faculty of Engineering, University of Porto, R. Dr. Roberto Frias, 4200-465 Porto, Portugal; ews@fe.up.pt (E.W.S.); rbns@fe.up.pt (R.F.S.); mvieira@fe.up.pt (M.F.V.)
- ² LAETA/INEGI, Institute of Science and Innovation in Mechanical and Industrial Engineering, R. Dr. Roberto Frias, 4200-465 Porto, Portugal
- ³ CCF—Associação Centro de Competências Ferroviário, Parque Oficinal de Guifões, Rua do Ferroviário, 4460-020 Matosinhos, Portugal
- * Correspondence: jose.costa@fe.up.pt

Abstract: While conventional die manufacturing techniques often lead to limitations in production speed and design intricacy due to labour-intensive procedures like machining and casting, Additive Manufacturing (AM) emerges as a key player offering substantial potential for cost reduction and process improvement in mass production. This study benchmarks four leading Laser Powder Bed Fusion (L-PBF) systems for producing maraging steel (EN 1.2709) dies. Despite the shared material and technology, variations in dimensional accuracy, surface finish, and microstructure were observed among the maraging steel parts. SEM/EDS, EBSD, hardness testing, and dimensional analysis revealed system-specific performance differences. Additionally, select parts underwent heat treatment and tensile testing, demonstrating the impact of post-processing on mechanical properties. These results offer valuable guidance for industrial stakeholders considering AM, highlighting the importance of supplier selection and process optimisation for achieving consistent part quality and unlocking the full potential of AM technologies.

Keywords: metal-based additive manufacturing; beam laser technologies; laser powder bed fusion; maraging steel



Citation: Costa, J.M.; Sequeiros, E.W.; Santos, R.F.; Vieira, M.F. Benchmarking L-PBF Systems for Die Production: Powder, Dimensional, Surface, Microstructural and Mechanical Characterisation. *Metals* **2024**, *14*, 520. <https://doi.org/10.3390/met14050520>

Academic Editor: Antonio Mateo

Received: 16 March 2024

Revised: 24 April 2024

Accepted: 25 April 2024

Published: 29 April 2024



Copyright: © 2024 by the authors. Licensee MDPI, Basel, Switzerland. This article is an open access article distributed under the terms and conditions of the Creative Commons Attribution (CC BY) license (<https://creativecommons.org/licenses/by/4.0/>).

1. Introduction

Traditional methods of die manufacturing often involve labour-intensive processes like machining and casting, leading to limitations in production efficiency and design complexity [1,2]. For example, intricate undercut features or complex internal cooling channels can be difficult or impossible to achieve, necessitating costly multi-part assemblies or extensive post-processing [3–7]. These limitations hinder innovation, leading to longer lead times and higher manufacturing costs [8,9]. Additive manufacturing (AM), particularly Laser Powder Bed Fusion (L-PBF), offers a transformative solution with its layer-by-layer fabrication approach [10–12]. L-PBF's ability to produce intricate designs and minimise material waste holds significant promise for optimising die production processes [13–15]. With its high strength, toughness, and widespread applications in tooling, maraging steel is a prime candidate for AM die manufacturing [16–19].

Despite the advantages of AM, the variability in outcomes across different L-PBF systems remains a significant obstacle to widespread industrial adoption [20–24]. Inconsistencies in dimensional accuracy, surface finish, microstructure, and mechanical properties can arise due to variations in equipment, process parameters, and material quality [25–27]. With standardisation, manufacturers can accurately assess the return on investment in

AM and justify the transition from established processes. This hinders the selection and optimisation of L-PBF processes for die production. In L-PBF systems (Figure 1), a layer of fine metal powder is uniformly spread in the machine bed by a recoater, either a blade or roller. A high-powered laser selectively melts a thin layer of metallic powder according to a CAD model [28,29]. The laser beam is guided by a scan head system, which precisely traces the part's geometry. After each layer is melted, a new layer of powder is deposited, and the process repeats. This layer-by-layer approach builds the part gradually, resulting in complex geometries with the desired properties [11,28]. This process ensures precise powder deposition and maintains consistent layer thickness throughout fabrication [30–32].

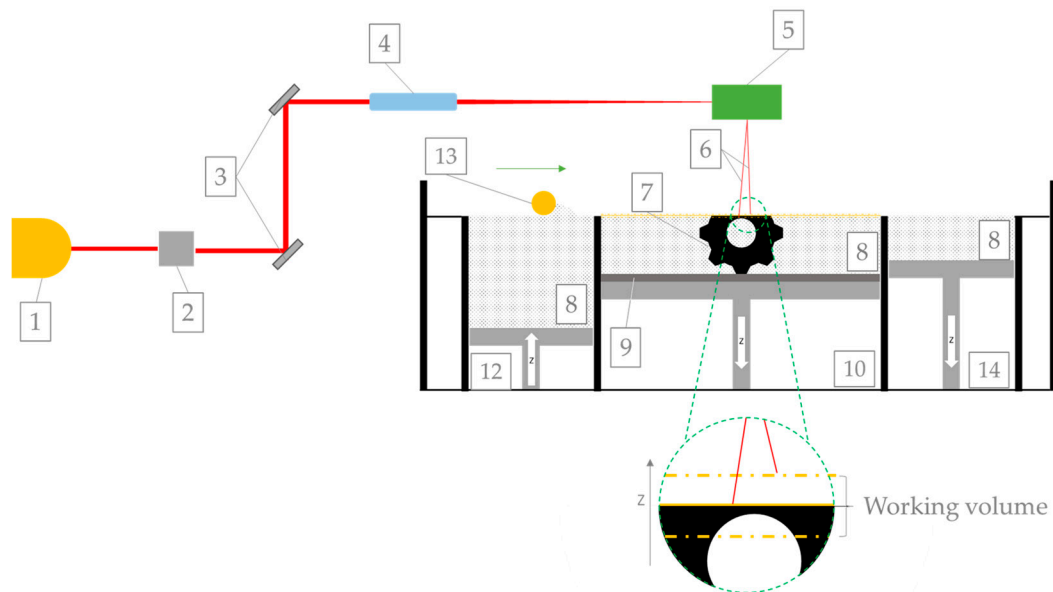


Figure 1. Schematic representation of the L-PBF system apparatus: (1) laser source, (2) beam expander, (3) adjustable mirrors, (4) Z-axis system, (5) scan head (or galvanometric scanner), (6) laser beam, (7) building part, (8) metallic powder, (9) build plate, (10) build compartment, (11) roller, (12) container of powder to be delivery system, (13) recoater, and (14) powder overflow container.

Recent benchmarking studies have begun to address L-PBF performance variations [15,33,34]. However, comprehensive research is still needed to focus on critical die manufacturing aspects, including dimensional accuracy, surface quality, microstructure, and mechanical properties. Such research would provide essential insights for industries considering AM technologies, guiding equipment selection and process optimisation. This research could significantly benefit the die manufacturing industry by advancing AM processes and standardisation. The ability to consistently produce complex, high-performance dies with AM could reduce production costs, shorten lead times, and enable new designs that would be impossible to manufacture with traditional methods. This would foster greater innovation and competitiveness within the industry.

This study aims to address these challenges by conducting a benchmarking analysis of multiple L-PBF systems specifically for die manufacturing. This study will meticulously evaluate these characteristics with and without post-build heat treatments. A unique aspect of this study is the in-depth investigation of heat treatment's impact on these critical performance metrics. This study aims to provide essential insights for industries exploring AM for die production, ultimately aiding in selecting optimal systems and processes. Our findings underscore the critical need for standardised process control methods to ensure consistent part quality across different AM platforms and emphasise the importance of understanding process parameter impacts on part quality across these platforms.

2. Materials and Methods

Investigating identical parts produced by four equipment manufacturers necessitates considering many factors, including part and process features and feedstock characteristics. This comprehensive analysis, represented in Figure 2, encompasses a range of critical parameters, including metallurgical characteristics (such as chemical composition and microstructure), mechanical properties (by hardness tests), and finishing aspects (such as surface roughness, distortion, and shrinkage).

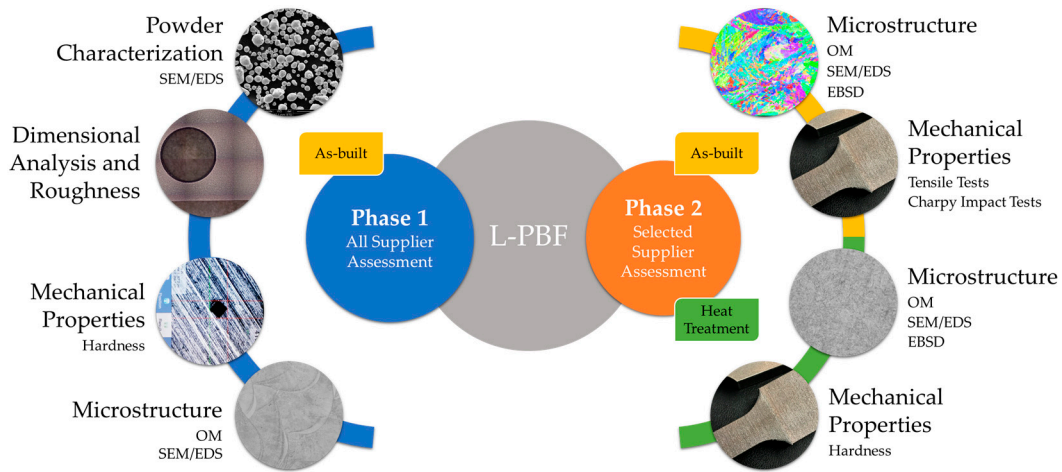


Figure 2. Work representation.

2.1. Phase 1 | Supplier Assessment: Powder and As-Built Parts Evaluation

2.1.1. L-PBF Process and Part Design

Key process parameters were provided as guidance (laser power 400 W, layer thickness 45 μm, etc.), with suppliers optimising other parameters based on their specific equipment and maraging steel powder characteristics (see Table 1).

Table 1. Key specifications of the L-PBF systems employed in the study.

Key Parameters	Supplier 1	Supplier 2	Supplier 3	Supplier 4
Build Volume	250 × 250 × 325 mm ³	280 × 280 × 350 mm ³	250 × 250 × 350 mm ³	300 × 300 × 400 mm ³
Laser Power	400 W	500 W	400 W	500 W
Scanning Speed	Up to 7.0 m/s	Up to 6.0 m/s	Up to 2.5 m/s	Up to 7.0 m/s
Layer Thickness	20–80 μm	20–50 μm	20–100 μm	20–100 μm
Laser Spot Size	50 μm	70 μm	30 μm	40 μm
Spot Spacing	100 μm	100 μm	80 μm	90 μm
Material Feed Rate	Up to 1000 mm ³ /h	Up to 500 mm ³ /h	Up to 300 mm ³ /h	Up to 800 mm ³ /h

Several factors drove the selection of specific L-PBF systems for comparison in this study to address critical gaps in current research and industry needs. The chosen systems represent a diverse range of commercially available L-PBF platforms commonly utilised in industrial settings. By comparing these systems, the focus is to provide comprehensive insights into the performance variability across different equipment types, thereby addressing the pressing need for standardised process control methods. Additionally, each selected system offers unique capabilities and operational characteristics, such as laser power, scanning speed, and build volume, which can significantly influence part quality and production efficiency. In line with maintaining impartiality and ensuring transparency, the identities of the selected equipment suppliers will be kept confidential. It is important to note that the intention is not to endorse any brand or assert superiority among equipment manufacturers. Instead, the focus remains on rigorous evaluation of the manufactured

parts to glean valuable insights into their performance and characteristics. To ensure reproducibility and facilitate understanding, pertinent specifications for each L-PBF system utilised in our study will be shared in Table 1.

All suppliers built four identical parts following the design specifications in Figure 3, oriented within the L-PBF machine as depicted in Figure 4.

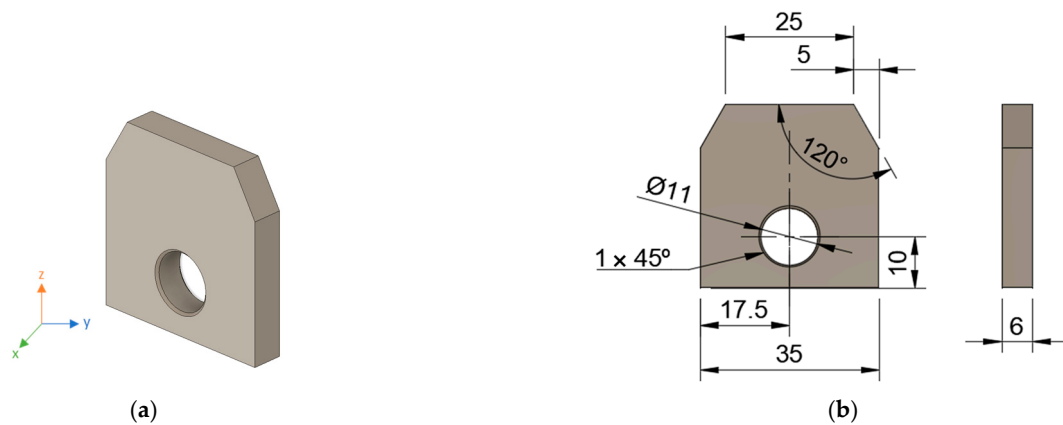


Figure 3. Representation of parts produced and used in the initial characterisations: (a) parts 3D design, and (b) parts dimensions in millimeters (mm).

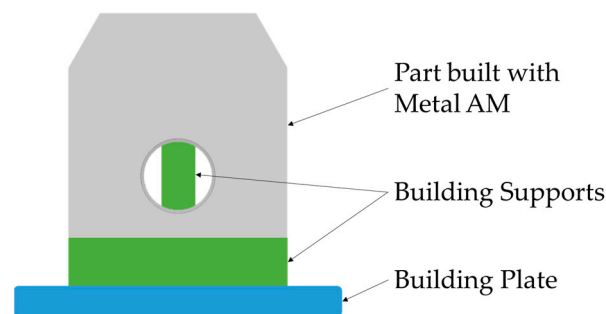


Figure 4. Illustration depicting the sample preparation for L-PBF, including support structures.

Initial parts were designed to support the phase 1 investigation (Figure 3). The parts designed for the initial phase have a parallelepiped shape, with two chamfers on the top and a hole (Figure 3a). The dimensions of the part are as shown in Figure 3b.

Initially, CAD 3D slicing (Fusion 360, Autodesk, San Francisco, CA, USA) was necessary to facilitate production via L-PBF. Each supplier used their own software to make production preparation parameters according to their equipment and software. However, it was indicated that parts should be produced according to the arrangement depicted in Figure 4. The suppliers strictly controlled process parameters, ensuring the desired characteristics and quality of the parts. The parameters provided to the suppliers as references included a laser power of 400 W, a layer thickness of 45 μm , and a preheating building platform temperature of 40 $^{\circ}\text{C}$, with the atmosphere controlled by nitrogen (Argon optional). Supplier experience, technical equipment capabilities, material properties, and part geometry considerations guided the determination of laser spot size and scan speed. While these parameters were initial guidelines, suppliers could adjust and optimise them to suit specific L-PBF technology applications. It is acknowledged that the precise settings of these parameters may vary based on material properties, machine manufacturers' recommendations, and the final parts' desired characteristics, highlighting the importance of supplier expertise and ongoing advancements in L-PBF technology.

2.1.2. Powder Characterisation

This comprehensive approach enabled a thorough characterisation of the maraging steel powder from all suppliers, shedding light on its physical properties, such as particle size, shape, and chemical composition, thus enhancing our understanding of its suitability for AM applications. The composition of maraging steel alloy is detailed in Table 2, underscoring its versatility and relevance across various industrial sectors.

Table 2. Composition of maraging steel (EN 1.2709) [18,35].

Alloying Element	Fe	Ni	Co	Mo	Ti	Al	Cr Cu	C	Mn Si	P S
wt%	Balance	17~19	8.5~9.5	4.5~5.2	0.6~0.8	0.05~0.15	≤0.5	≤0.03	≤0.1	≤0.01

A particle size and shape analysis was conducted using scanning electron microscopy (SEM) (Thermo Fischer Scientific Quanta 400FEG ESEM, Waltham, MA, USA) coupled with energy-dispersive X-ray spectroscopy (EDS) (EDAX Genesis X4M, AMETEK, Berwyn, PA, USA); spectra were used to determine chemical composition to complement the evaluation of maraging steel powder from each supplier. Maraging steel powder was analysed using the high-resolution SEM images (Thermo Fischer Scientific Quanta 400FEG ESEM, Waltham, MA, USA), and EDS analysis was accessed using the FEI Quanta 400 FEG ESEM/EDAX Genesis X4M (Thermo Fischer Scientific Quanta 400FEG ESEM, Waltham, MA, USA/EDAX Genesis X4M, AMETEK, Berwyn, PA, USA) of high resolution (Schottky). Particle size distribution and morphology were measured using ImageJ software (version 1.51p, National Institutes of Health, Bethesda, MD, USA).

2.1.3. Dimensional Analysis

A thorough study was conducted on factors affecting dimensional accuracy, including part orientation, scan strategy, and manufacturing parameters. A DVM6 Digital Microscope (Leica DVM6, Leica Microsystems GmbH, Wetzlar, Germany) captured high-resolution images for dimensional analysis, and ImageJ software was used for precise measurements. Dimensions measured are shown in Figure 5, with a tolerance of ± 0.10 mm.

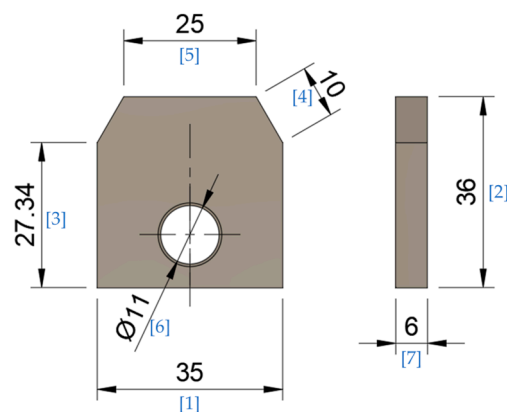


Figure 5. Controlled dimensions of the L-PBF specimens in millimeters (mm).

2.1.4. Surface Roughness

Surface roughness analysis of maraging steel parts from suppliers 1 to 4 was conducted according to the ISO 4287 standard [36]. This standard specifies key parameters for characterising surface morphology, including Arithmetic Mean Deviation (R_a), Mean Square Deviation (R_q), Maximum Profile Height (R_z), Asymmetry Factor (R_{sk}), and Flatness Factor (R_{ku}).

The Leica DVM6 Digital Microscope, equipped with a magnification objective (maximum field of view of 12.55 mm, 50 \times magnification), was employed for precise surface

measurements. Leica LAS X software was used for 2D and 3D image acquisition. Leica Map Start software (Leica Map Start, Leica Microsystems GmbH, Wetzlar, Germany) enabled 3D surface visualisation, feature characterisation, and calculation of surface texture parameters according to the standard.

2.1.5. Microstructural Analysis

As-built parts from suppliers 1–4 were prepared for metallographic analysis. Cross-sections in both XY and Z orientations (see Figure 6) were cut, ground, and polished to a final finish of 0.03 μm using colloidal silica.

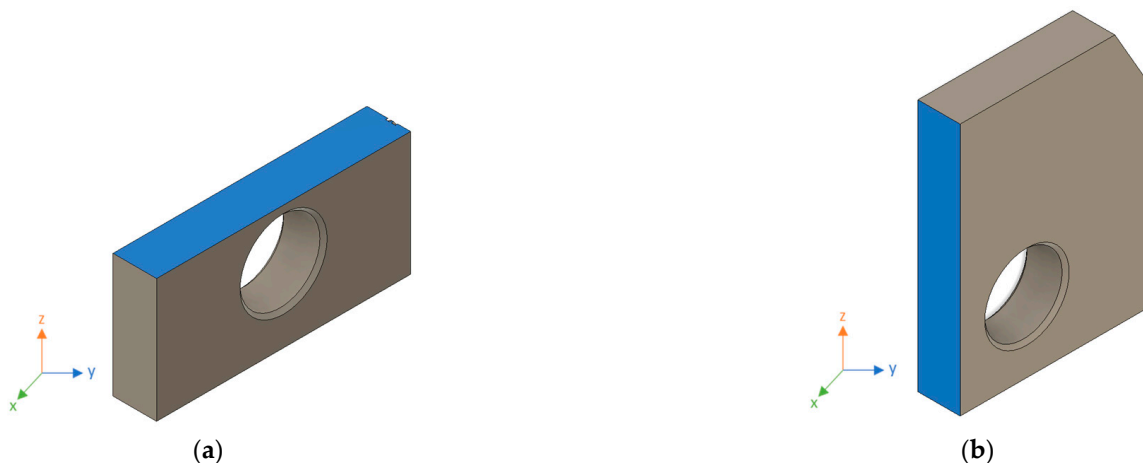


Figure 6. Cross-section representation of XY (a) and Z (b) in parts used in the initial characterisations.

Optical microscopy (OM) (Leica DM 4000M, Leica Microsystems GmbH, Wetzlar, Germany) was performed using a Leica DM 4000M microscope equipped with Leica Las software. Before examination, specimens were etched with a solution of Picral 4% plus Nital 2% to reveal microstructural features. Scanning electron microscopy coupled with energy-dispersive X-ray spectroscopy (SEM/EDS) was performed for higher resolution analysis and elemental composition determination using a Thermo Fischer Scientific Quanta 400FEG ESEM (Waltham, MA, USA), and EDAX Genesis X4M (Schottky) (AMETEK, Berwyn, PA, USA).

2.1.6. Hardness Testing

Vickers hardness tests were performed on XY and Z cross-sections of as-built parts according to ISO 6507-1:2005 [37]. Measurements were made using an indenter load of 100 mN for 15 s with Duramin 5 software (Struers, Ballerup, Hovedstaden, Denmark). Twenty indentations were performed on each specimen.

2.2. Phase 2 | Selected Supplier: Further Characterisation and Evaluation and Heat Treatments HT

The supplier demonstrating the best overall performance in Phase 1 was selected for further analysis. Performance was evaluated based on key metrics, including dimensional accuracy, surface finish, microstructure, and hardness. Additional evaluations were conducted: strength and impact tests, electron backscatter diffraction (EBSD) (AMETEK, Berwyn, PA, USA), and heat treatments (HT). The HT samples include microstructural analysis and hardness tests.

2.2.1. Heat Treatments

The mechanical properties of maraging steel are predominantly determined by its heat treatment process, which leads to the precipitation of intermetallic phases, consequently enhancing its mechanical properties, like tensile strength, hardness, ductility, toughness, wear resistance, and strength [35,38,39]. Maraging steel typically undergoes a thermal

ageing treatment to enhance its mechanical properties, which is especially crucial in the context of the L-PBF process. HTs were performed in the best supplier part, solubilisation (S) and ageing (A). Solubilisation (S) at 850 °C for 1 h, followed by air cooling. Subsequently, the age-hardening (A) was performed with a heating rate of 100 °C/h with a stage at 540 °C for 6 h, followed by furnace (Termolab, Águeda, Portugal) cooling (Figure 7). The effect of performing and not performing solubilisation was studied; SA and A samples were analysed microstructurally and tested (hardness tests were accessed as described in phase 1).

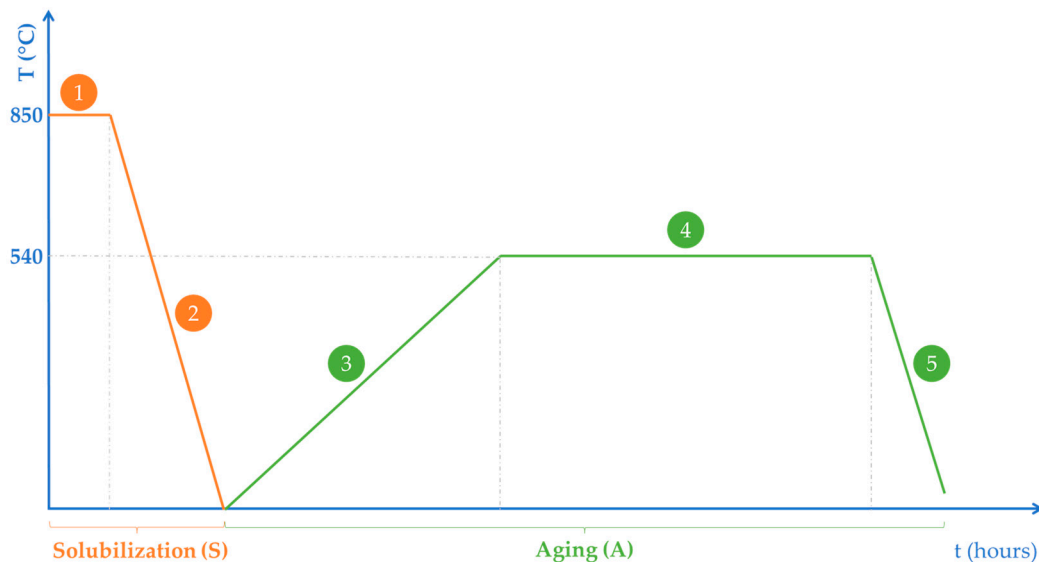


Figure 7. Thermal cycle for solubilisation (S) and ageing (A) of maraging steel parts. (1) One hour at 850 °C, (2) air cooling, (3) 100 °C/hour, until T540 °C, (4) 8 h at 540 °C, (5) cooling inside furnace.

2.2.2. Tensile Testing

Six tensile test specimens (Figure 8a) with gauge dimensions of $10 \times 10 \times 55 \text{ mm}^3$ (Figure 8b) were fabricated in two orientations. Three specimens were built with the longer axis parallel to the building direction (Z, Figure 8d), and the other three were built with longer and shorter axes parallel to the powder bed (XY, Figure 8d). The ISO 6892-1:2012B [40] with a Shimadzu UH 1000KN (Shimadzu, Kyoto, Japan) performed the tensile tests.

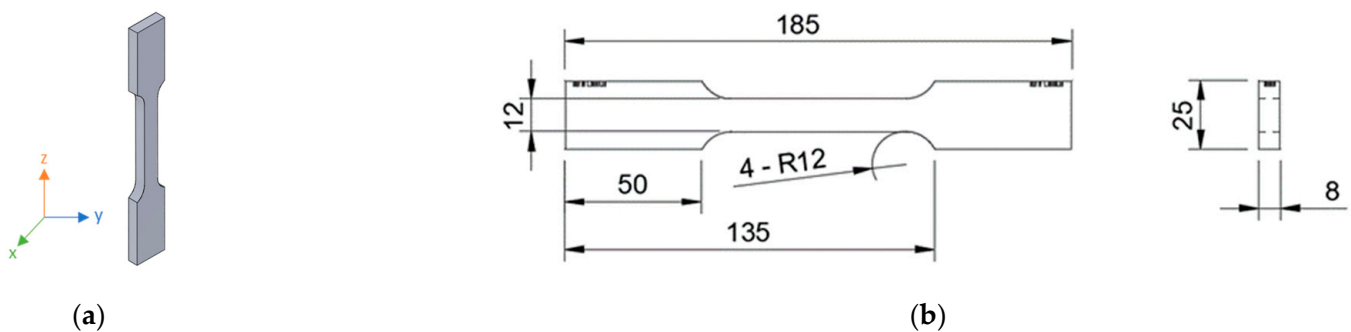


Figure 8. Cont.

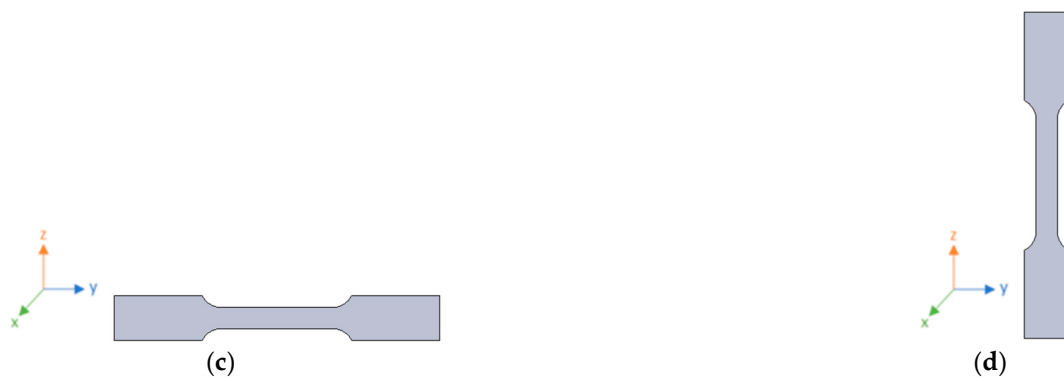


Figure 8. Tensile test samples (a) with $8 \times 12 \times 185 \text{ mm}^3$ gauge dimensions (b) and representation of XY (c) and Z (d) in millimeters (mm).

2.2.3. Impact Testing

Eight Charpy-V notch specimens (Figure 9a) with gauge dimensions of $10 \times 10 \times 55 \text{ mm}^3$ (Figure 9b) were fabricated in two orientations. Four specimens were built vertically, aligning the longer axis parallel to the building direction (Z, Figure 9d), and the remaining four were constructed with longer and shorter axes parallel to the powder bed (XY, Figure 8c). Impact tests were conducted according to ISO 148-1 standards [41], with evaluations performed under both as-built and aged conditions (described next). Two specimens from each orientation (XY and Z) were tested in each condition.

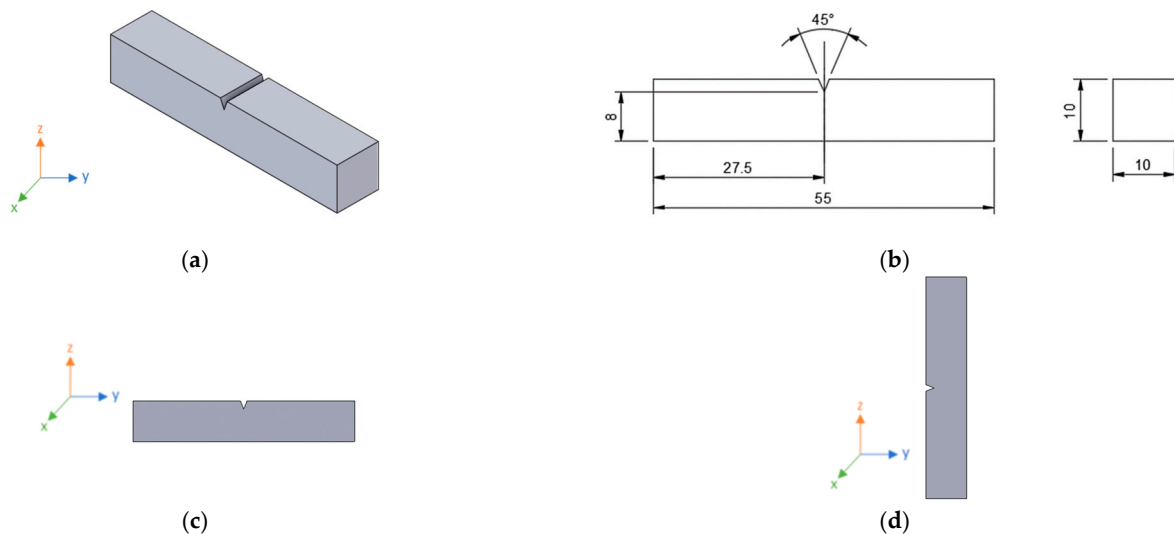


Figure 9. Standard Charpy-V notch specimen (a) with $10 \times 10 \times 55 \text{ mm}^3$ gauge dimensions (b) and representation of XY (c) and Z (d) in millimeters (mm).

The specimens were manufactured, including the V notch. As the examples shown in Figure 10 show, the notch did not meet the requirements (2 mm depth, 45° angle, and 0.25 mm tip radius). Specimens were refurbished to obtain these dimensions.

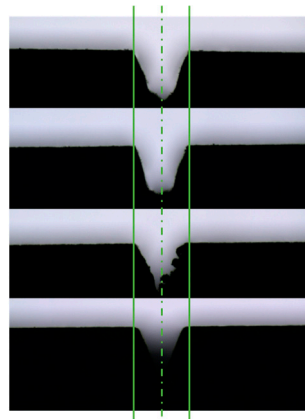


Figure 10. Examples of V notch obtained in specimens produced in this project.

2.2.4. EBSD

EBSD mapping was performed on a $60\ \mu\text{m}^2$ area on both sections, XY and Z for supplier 1, using a hexagonal grid with a step of $0.6\ \mu\text{m}$. Datasets were processed using OIM Analysis software (version 5.2, AMETEK, Berwyn, PA, USA). The following clean-up routines were applied: (1) neighbour CI correlation ($\text{CI} > 0.15$) and (2) grain dilation with minimum grain size of 6 pixels ($\sim 1.87\ \mu\text{m}^2$) and minimum grain tolerance angle of 5° .

3. Experimental Results and Discussion

3.1. Phase 1 | Supplier Assessment: Powder and As-Built Parts Evaluation

3.1.1. Powder Analysis

A thorough analysis of powders from all suppliers revealed a predominantly spherical or near-spherical shape without sharp edges, crucial for good flowability in L-PBF processes. Particle sizes ranged from 6 to $60\ \mu\text{m}$, averaging $30\ \mu\text{m}$ (Figure 11).

This size distribution is within the typical range for L-PBF maraging steel [42,43], ensuring appropriate melt pool formation. However, some minor deviations in powder characteristics between suppliers were noted. Supplier 2 exhibited a higher presence of clusters composed of coalesced particles, while supplier 1 had occasional elongated particles exceeding $60\ \mu\text{m}$ in length. Such variations in particle morphology could potentially influence powder packing density and melt pool dynamics during the L-PBF process.

EDS analysis indicated the presence of oxide inclusions rich in oxygen, aluminium, and titanium on the particle surfaces of all suppliers' powders (Figure 12). Figure 12 presents the analysis for supplier 1, with an SEM image (Figure 12a) and EDS spectrum of the powders (Figure 12b, Z6) and inclusions (Figure 12c, Z7), as an example of the powders from suppliers 2, 3 and 4.

These inclusions are commonly observed in gas-atomised metal powders [44,45]. Although their presence could raise concerns about final part properties, their overall chemical composition aligns with expectations for maraging steel powders (Table 3).

Table 3. EDS quantification of powder particles (P) and inclusions (I) for each supplier.

Alloying Element (wt%)	C	O	Mo	Ti	Fe	Co	Ni	Al
Supplier 1 (P)	0.48	1.91	4.96	1.36	66.73	7.57	16.99	7.13
Supplier 1 (I)	0.84	40.01	-	46.69	4.25	1.08	-	-
Supplier 2 (P)	0.53	-	5.72	1.44	64.92	9.42	-	-
Supplier 2 (I)	0.75	17.34	4.31	2.44	38.19	5.83	10.67	20.48
Supplier 3 (P)	0.69	1.41	5.14	0.75	66.15	8.51	17.35	-
Supplier 3 (I)	-	25.87	-	50.49	13.24	-	2.7	7.7
Supplier 4 (P)	0.51	-	5.5	1.31	64.43	9.99	18.26	-
Supplier 4 (I)	0.88	26.62	2.79	12.9	20.92	2.9	4.52	28.46

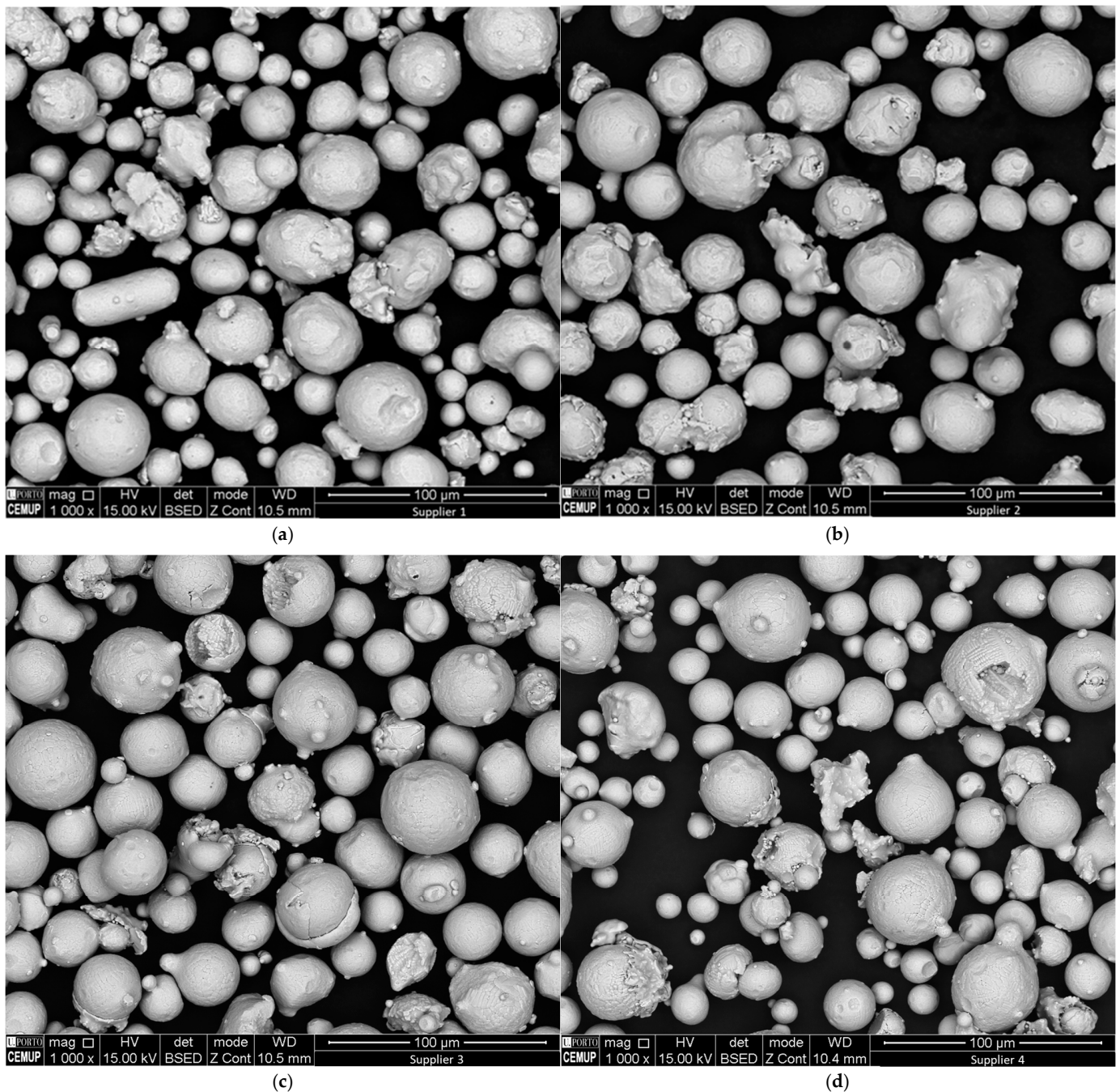


Figure 11. SEM image of the maraging steel powders used in this study from suppliers (a) 1, (b) 2, (c) 3, and (d) 4.

Overall, the powders used by all suppliers exhibited characteristics that were generally suitable for L-PBF processing. However, the observed subtle differences in particle morphology and inclusion content highlight the potential for variations in powder bed behaviour and differences in melt pool formation and solidification. These differences may contribute to the variations in surface quality, dimensional accuracy, and microstructure observed among the suppliers' parts, a crucial point to explore further in the upcoming sections.

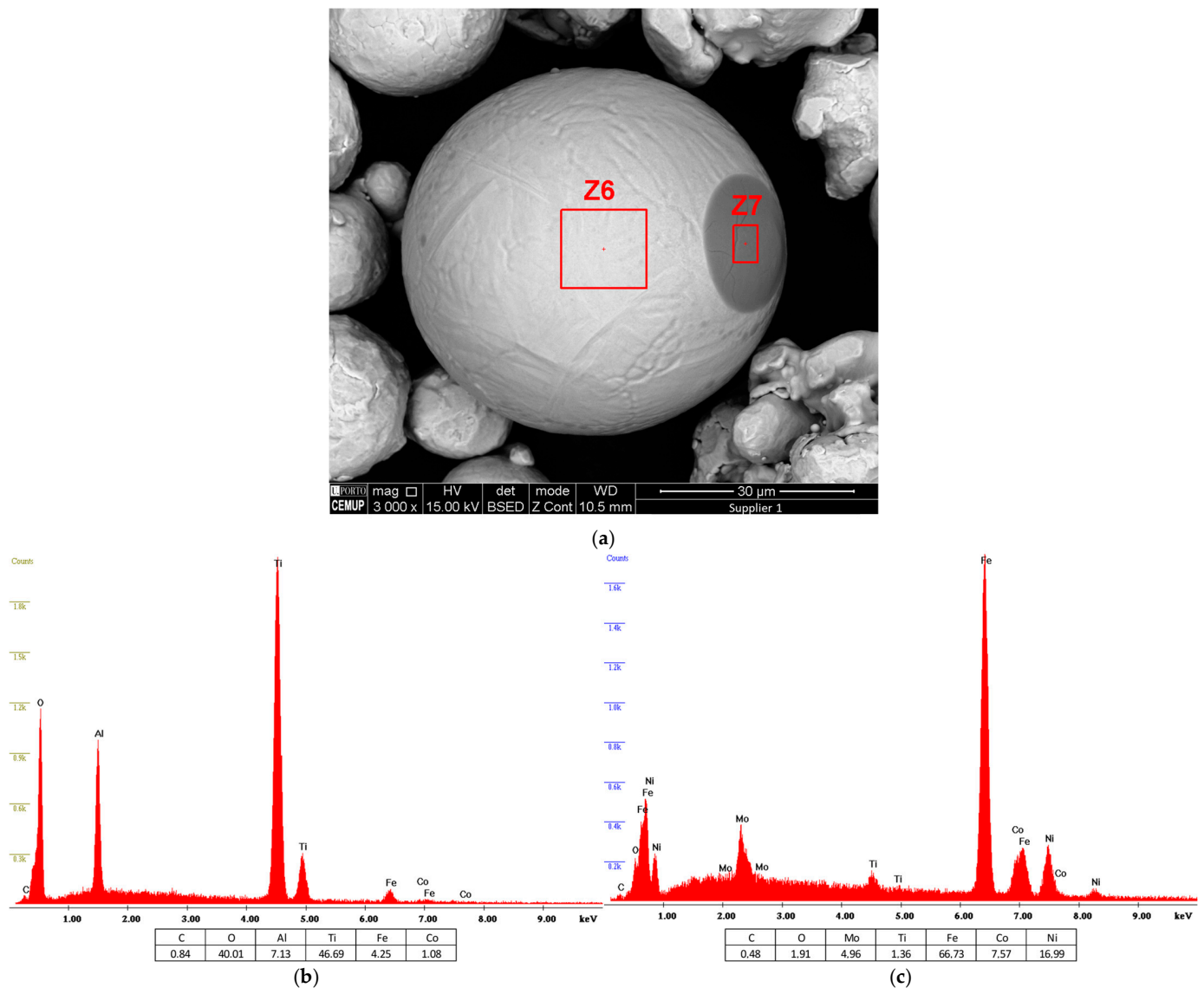


Figure 12. SEM analysis of supplier 1 maraging steel powder (a), and the result of EDS analysis for Z6 (b) and EDS analysis for inclusion Z7 (c).

3.1.2. Dimensional Accuracy

Dimensional analysis (Table 4) revealed significant differences in accuracy among parts produced by the four suppliers. Supplier 1 demonstrated superior performance, with measurements consistently falling within the specified tolerance limits for dimensions 1, 4, 5, 6, and 7. Conversely, suppliers 2 and 4 exhibited substantial deviations, indicative of part distortion. Supplier 3, while slightly exceeding tolerances, was closer to the acceptable range. The interconnected nature of dimensions 2 and 3 likely amplifies discrepancies when distortions occur.

These findings highlight the complex influence of L-PBF process parameters on dimensional accuracy. Variations in laser power, scanning strategy, hatch spacing, or layer thickness between suppliers can induce different thermal gradients within the part during the build. These thermal gradients can cause uneven shrinkage and distortion, leading to the observed dimensional inaccuracies [46–48]. Moreover, the presence of build supports and their geometry, while necessary, can introduce additional variability due to their interaction with the part as it is being manufactured.

Methodology refinement is necessary further to improve the reliability of dimensional analysis for L-PBF parts. Dedicated metrology equipment specifically designed for complex

AM geometries would provide more precise evaluations of distortion and shrinkage [49,50]. Addressing these challenges is crucial for optimising AM processes and ensuring consistent dimensional quality.

Table 4. Dimensional analysis. Measure 1 to 7 (description available in Figure 5).

Reference Dimension	Supplier 1		Supplier 2		Supplier 3		Supplier 4		
	Dimension (mm ³)	Tolerance (±0.10 mm)	Dimension (mm ³)	Tolerance (±0.10 mm)	Dimension (mm ³)	Tolerance (±0.10 mm)	Dimension (mm ³)	Tolerance (±0.10 mm)	
1	35.00	34.91	−0.09	34.83	−0.17	34.95	−0.05	34.84	−0.16
2	36.00	36.55	0.55	36.28	0.28	36.30	0.30	35.89	−0.11
3	27.34	27.84	0.50	27.73	0.39	27.72	0.38	27.2	−0.14
4	10.00	9.98	−0.02	10.23	0.23	10.01	0.01	10.02	0.02
5	25.00	25.07	0.07	24.83	−0.17	24.88	−0.12	24.78	−0.22
6	11.00	11.03	0.03	10.85	−0.15	10.89	−0.11	10.89	−0.11
7	6.00	5.98	−0.02	6.04	0.04	6.06	0.06	5.86	−0.14

3.1.3. Surface Roughness

Surface roughness plays a crucial role in the overall quality of L-PBF parts, influencing dimensional accuracy and critical performance aspects like fatigue strength and surface finish [48,51]. Leica software enabled roughness analysis, and Figure 13 presents an example of how it is given in the data collected, in this case for supplier 1. The study revealed that suppliers 1 and 4 achieved similar Ra values (Table 5), which were significantly lower than those of suppliers 2 and 3. This aligns with expectations from the literature [48] for metal AM parts. However, supplier 1 consistently demonstrated the best surface finish among all suppliers.

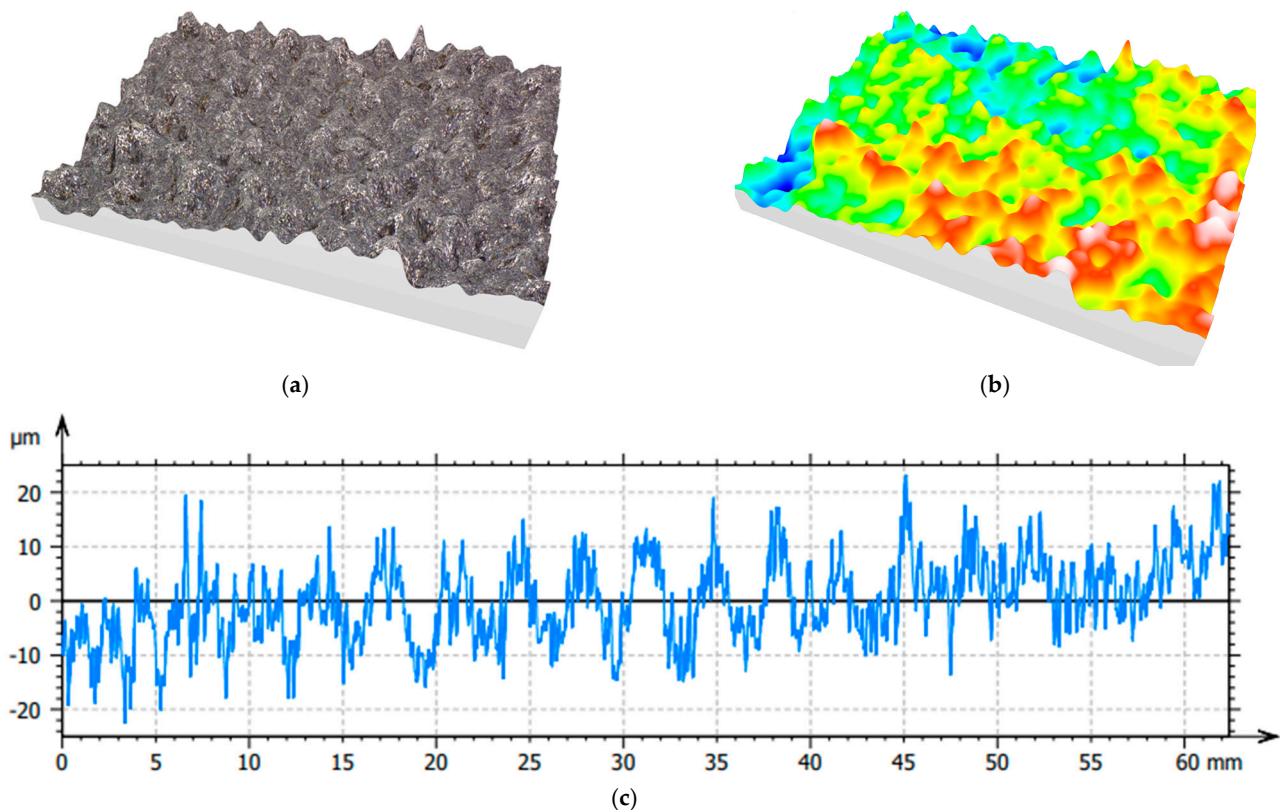


Figure 13. Roughness analysis of the specimen surface of supplier 1, showing the topography of surfaces (a), 3D visualisation of the analysed surface (b), and the roughness profile evaluated (c).

Table 5. Roughness dimensions attained.

	Supplier 1	Supplier 2	Supplier 3	Supplier 4
R_a (μm)	2.5	4.0	4.3	2.8
R_q (μm)	3.1	4.9	5.2	3.5
R_z (μm)	12	20	20	14
R_{sk}	0.11	0.10	0.08	0.36
R_{ku}	2.5	2.7	2.5	2.9

Process parameters and powder characteristics likely underlie these observed differences. The solidification behaviour of the melt pool is strongly influenced by factors like laser power, scanning strategy, and layer thickness, all of which can impact surface roughness [51–54]. Additionally, variations in powder particle morphology (noted in the Section 3.1.1) could contribute. Coarser or irregular particles tend to increase surface roughness [48].

The surface roughness analysis is presented in Table 5 for all suppliers. Suppliers 1 and 4 exhibit similar R_a values, with a slight difference of approximately $0.3 \mu\text{m}$, significantly smaller than parts from suppliers 2 and 3, which also have a difference of $0.3 \mu\text{m}$, with the highest R_q deviation. The surface characteristics of the analysed parts provide further insights. Positive R_{sk} values and R_{ku} values under three for all suppliers suggest the presence of a surface dominated by peaks rather than valleys. These metrics are essential for applications where surface contact and friction play a role. Gibson et al. [48] suggest that acceptable R_a falls within the range of 4 to $6.5 \mu\text{m}$. In comparison, R_z falls within the range of 20 to $50 \mu\text{m}$, inferring that suppliers 1 and 4 have values below, indicating superior quality compared to suppliers 2 and 3. Regarding R_z , suppliers 1 and 4 are below the reference values again, and suppliers 2 and 3 are within the limits.

Understanding and controlling surface roughness is essential in L-PBF, particularly for industries with strict surface quality requirements. Surface defects from roughness act as stress concentrators, promoting fatigue crack initiation, reducing die lifetime, and increasing costly downtime for replacement [52,55]. Optimising L-PBF process parameters and ensuring powder quality is crucial for achieving the desired surface characteristics, enhancing fatigue resistance, and ensuring the suitability of parts for their intended applications.

3.1.4. Microstructure

Optical microscopy (OM) analysis of all suppliers' parts revealed characteristic microstructural features of L-PBF maraging steel (Figure 14). The presence of overlapping melt pools (XY direction) and laser scan tracks (Z direction) reflects the layer-wise build process employed in L-PBF. Suppliers have used varying scanning strategies, as evidenced by differences in melt pool sizes and scan track patterns. These strategic variations reduce porosity and internal stresses within the manufactured parts.

A closer examination highlights microstructural variations between suppliers. Except for supplier 2, the microstructures generally reveal fine cellular and columnar grains growing perpendicular to the melt pool boundaries along the build direction. This grain morphology is typical of L-PBF maraging steel and results from the rapid solidification conditions [17,19,38]. In contrast, supplier 2 exhibits a fine microstructure without clear cellular or dendritic features, potentially indicating a different thermal history during processing. This might be due to a strategy involving reheating or extended laser exposure time after the deposition of each layer.

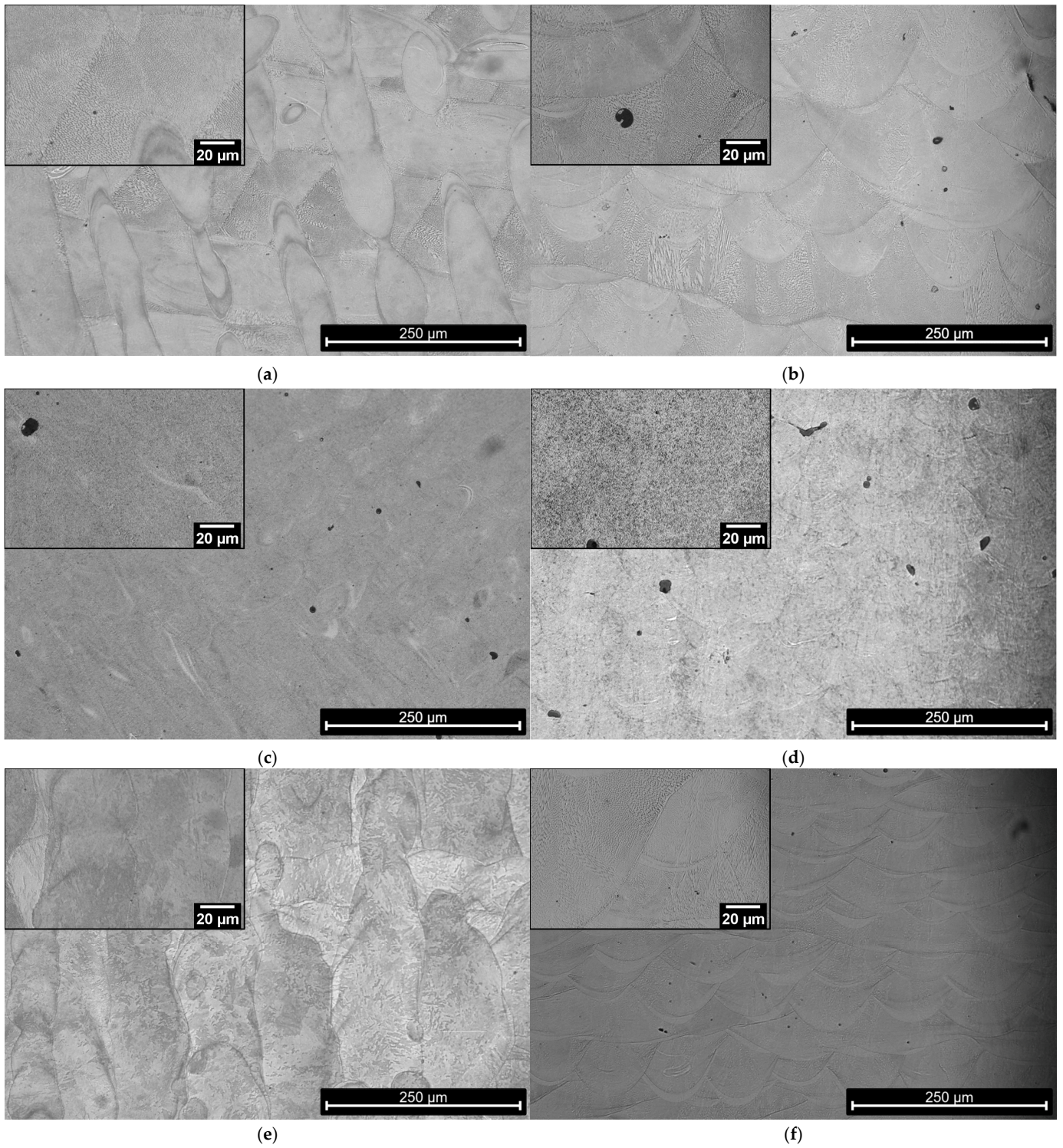


Figure 14. Cont.

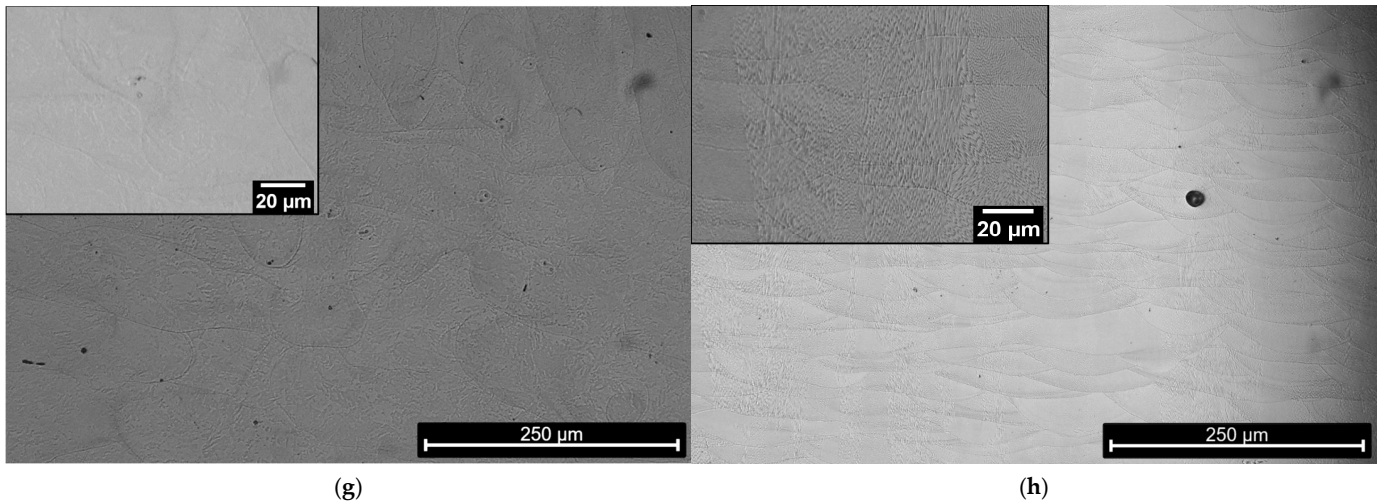


Figure 14. Cross-section images at OM of the four as-built parts for supplier 1 ((a). XY, (b). Z), supplier 2 ((c). XY, (d). Z), supplier 3 ((e). XY, (f). Z), and supplier 4 ((g). XY, (h). Z).

SEM analysis (Figure 15) further confirmed microstructural similarities between suppliers 1, 3, and 4, consisting of fine martensitic structures with precipitates, as expected for maraging steel under rapid cooling conditions [16,38,56]. The differences in grain morphology observed under OM are likely due to subtle variations in cooling rates and thermal gradients experienced during the build, influenced by supplier-specific process parameters.

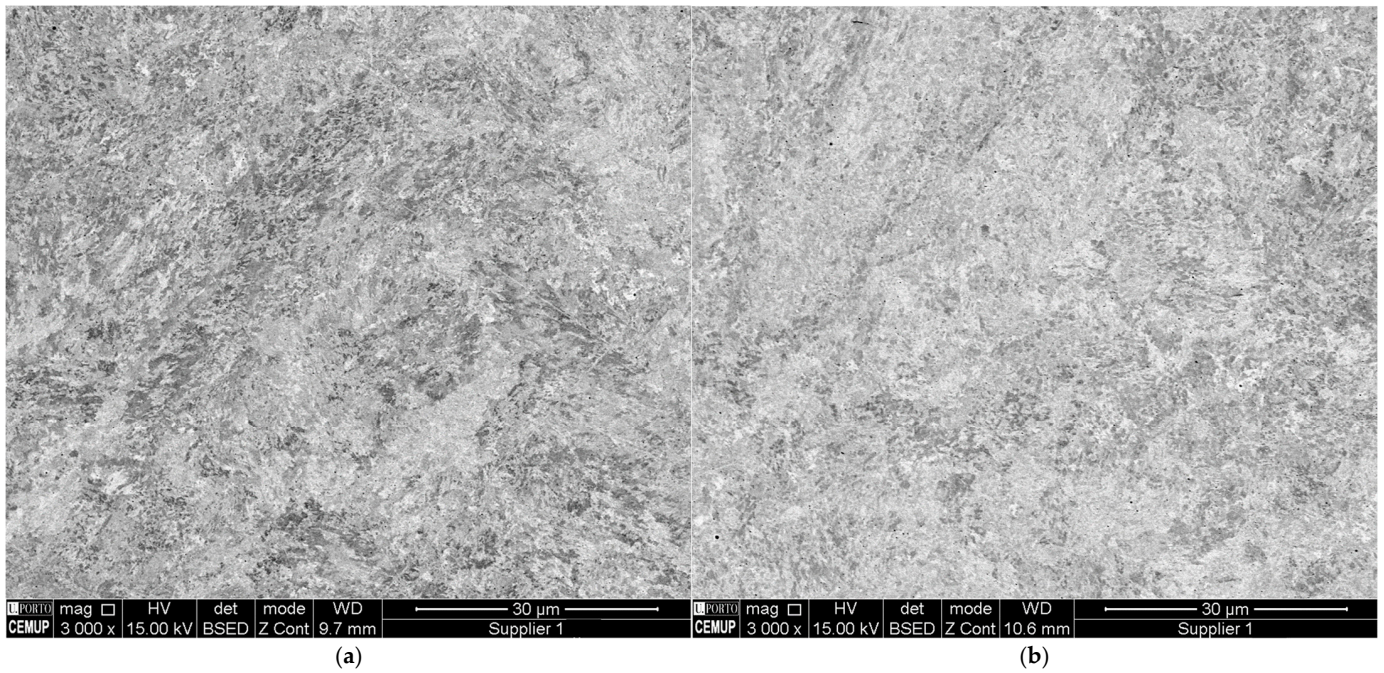


Figure 15. Cont.

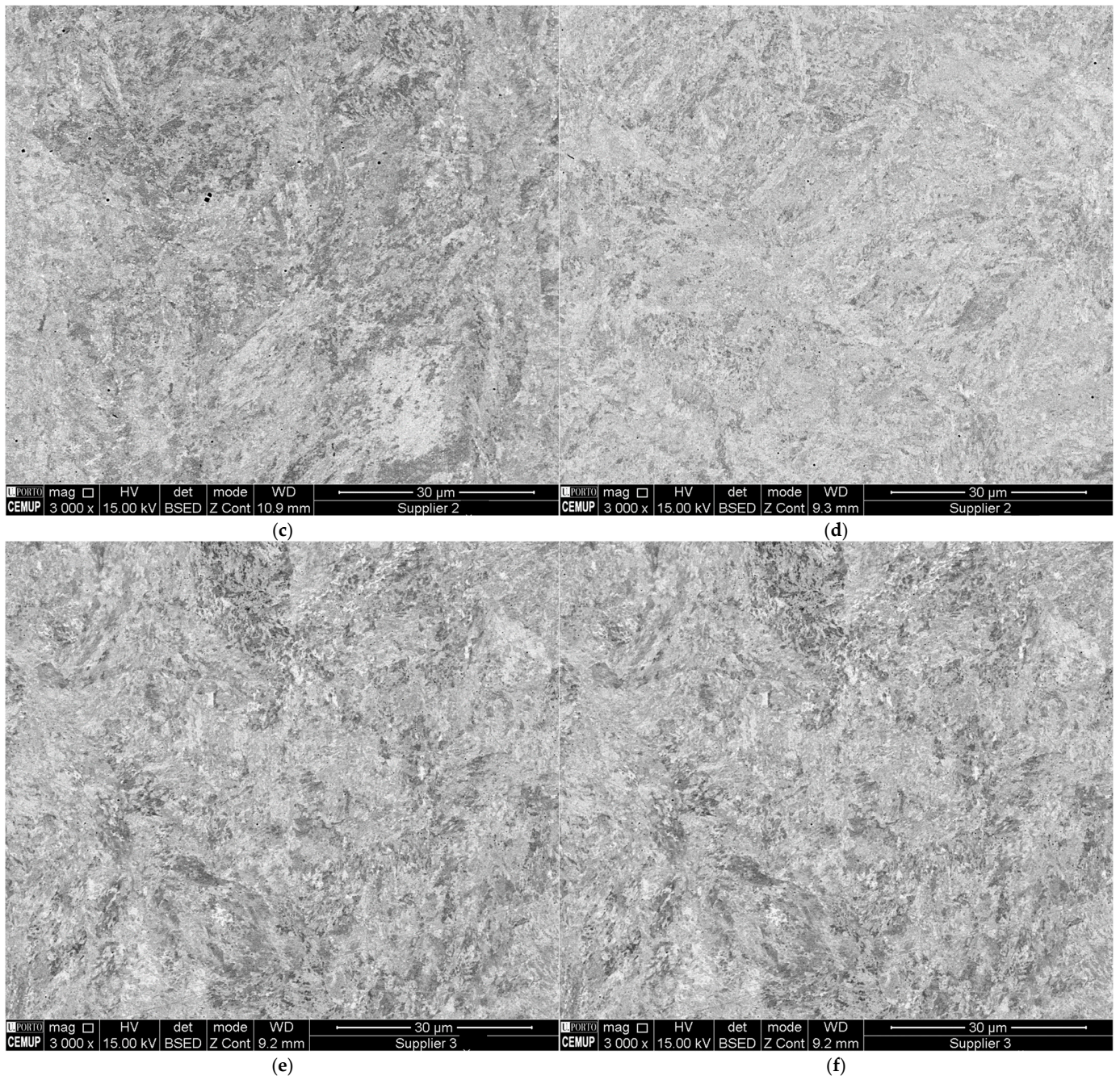


Figure 15. Cont.

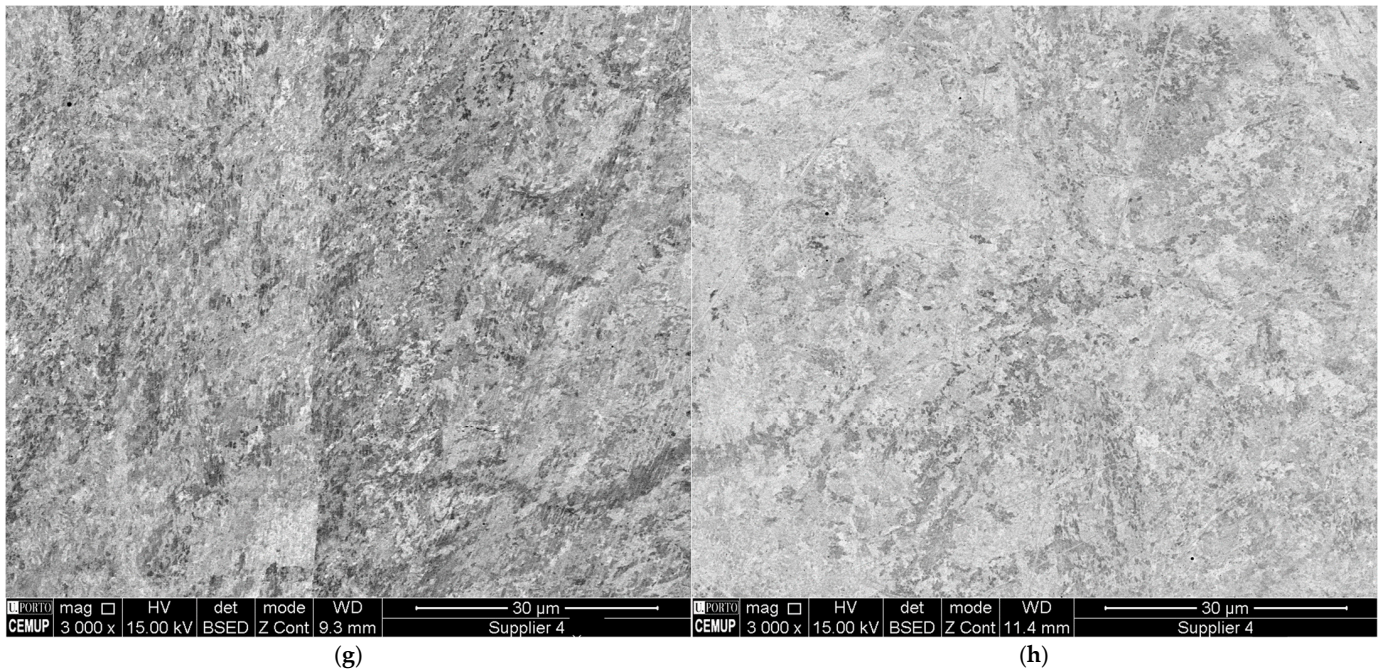


Figure 15. Maraging steel SEM microstructure for the four parts for supplier 1 ((a). XY, (b). Z), supplier 2 ((c). XY, (d). Z), supplier 3 ((e). XY, (f). Z), and supplier 4 ((g). XY, (h). Z).

EDS analysis revealed inclusions rich in titanium, aluminium, and oxygen, likely oxides (Figure 16), which is consistent with the literature’s findings on maraging steel [16,18]. The EDS spectrum of the Z1 area (Figure 16a–c) and the Z3 area (Figure 16d) revealed titanium, aluminium, and oxygen, enabling the titanium and aluminium combined oxides ($TiO_2:Al_2O_3$). Supplier 3 demonstrated the smallest quantity and size of inclusions, while supplier 2 showed the most inclusions aligned along the laser scan direction. The variances in inclusion characteristics suggest potential differences in powder quality (as seen in point 3.1.1) and oxygen control during the L-PBF process.

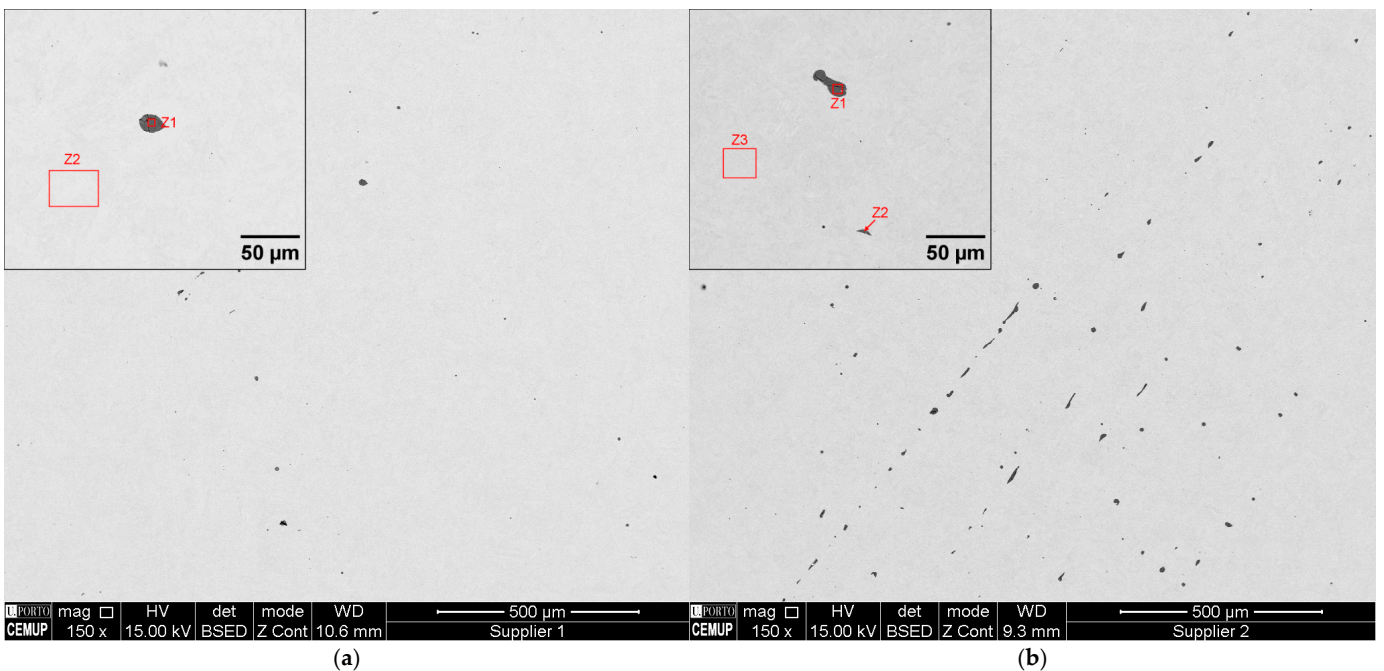


Figure 16. Cont.

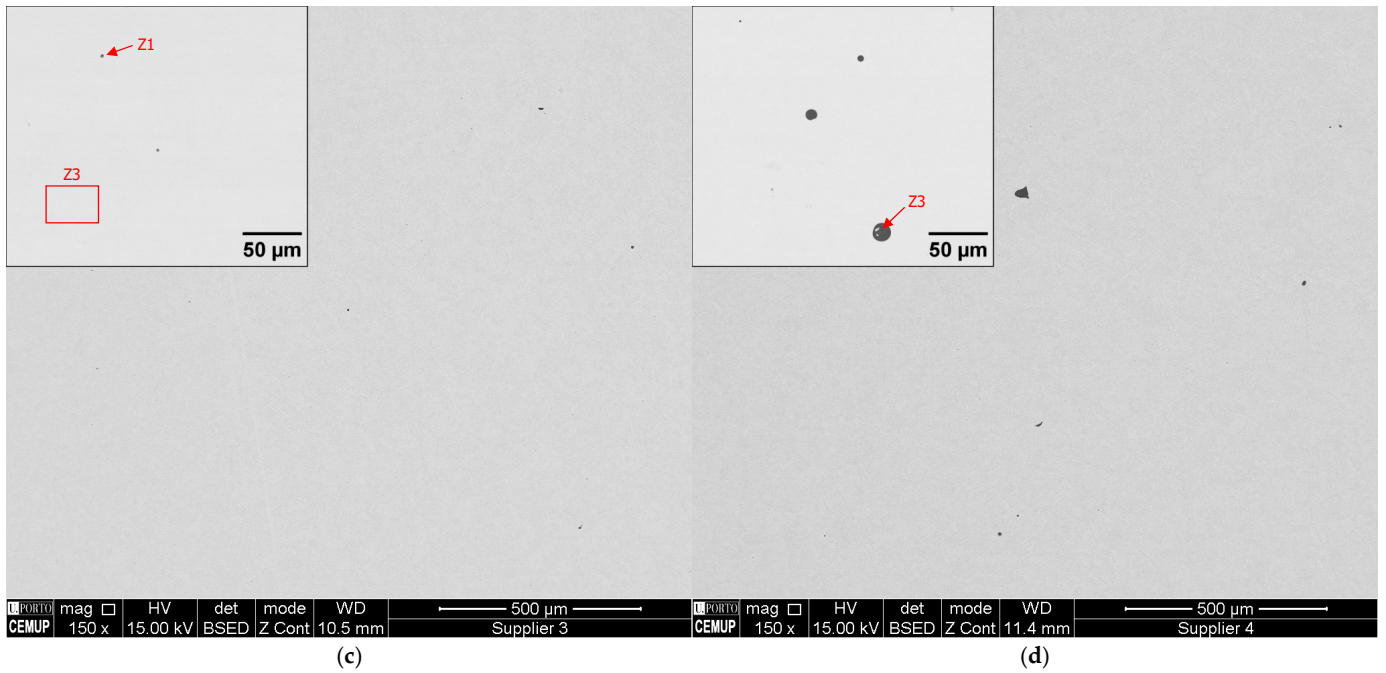


Figure 16. Inclusions for suppliers 1, 2, 3, and 4. (a–c) the EDS spectrum of the Z1 area and (d) the Z3 area.

3.1.5. Hardness

Hardness testing provided valuable insights into the mechanical properties of the L-PBF-produced maraging steel parts, indicating their suitability for industrial applications. The hardness values across the four suppliers exhibited variations (Figure 17). Supplier 1 demonstrated the highest average Vickers hardness (XY: 371 ± 13 HV, and Z: 388 ± 17 HV), while suppliers 2, 3, and 4 exhibited lower average values (between 340 and 360 HV to XY, and 360 and 380 HV). These variations suggest that even subtle differences in L-PBF process parameters can significantly impact the mechanical characteristics of the final parts.

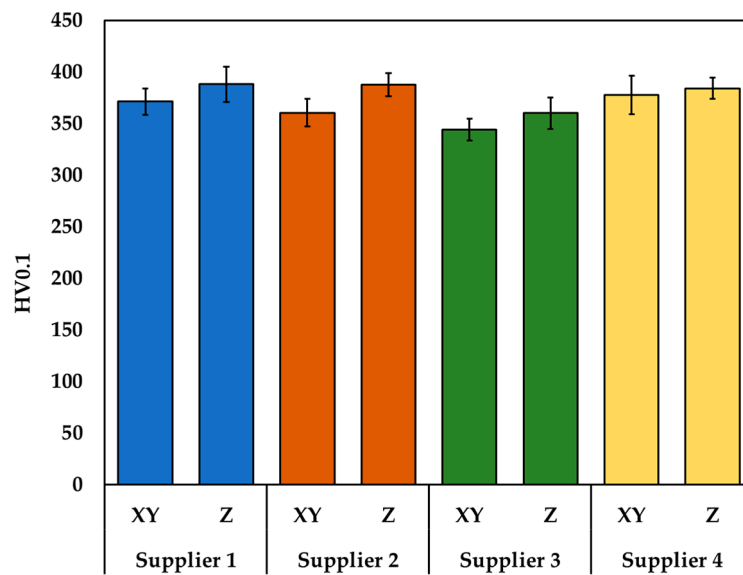


Figure 17. Hardness measurements were obtained in the as-built condition on longitudinal (XY) and transverse (Z) sections.

3.2. Phase 2 | Selected Supplier: Further Characterisation and Evaluation and Heat Treatments HT

The inherent layer-by-layer nature of L-PBF introduces microstructural anisotropy that can influence hardness and other mechanical properties [57–59]. Variations in thermal gradients during the build process, influenced by process parameters, can lead to localised grain structure and precipitate distribution differences. Understanding how specific L-PBF process parameters impact hardness is crucial for optimising parts for specific industrial applications. Maraging steel's well-known corrosion resistance [19,54,60] remains an additional advantage of this class of alloys for demanding applications.

The initial assessment phase employed a comprehensive suite of analyses, including dimensional measurements, surface roughness evaluation, and hardness testing, to assess the mechanical properties of L-PBF fabricated parts for industrial applications. While all parts utilised the same maraging steel material and L-PBF technology, clear distinctions emerged among the suppliers. Supplier 1's parts consistently surpassed expectations in critical areas. Dimensional analysis revealed exceptional accuracy, consistently meeting specified tolerances. Surface roughness analysis confirmed excellent surface quality, exceeding industry standards for similar dies. Microstructure examinations further bolstered these positive findings, showcasing fine martensitic structures and precipitates the characteristics of high-performance maraging steel. These combined results highlight the significant influence that process parameter variations can exert on final part properties. Consequently, the part manufactured by supplier 1 was chosen for in-depth mechanical testing in Phase 2. This strategic selection leverages the part's demonstrated superiority in dimensional accuracy, surface finish, and microstructure, offering the highest potential for meeting the performance demands of industrial applications. Phase 2 adds additional evaluations of the mechanical behaviour of this supplier, evaluating its performance in both as-built and in HT conditions. This analysis aims to elucidate the intricate relationships between L-PBF process parameters, microstructure development, and resulting mechanical properties, ultimately paving the way for optimising L-PBF parts for industrial success.

3.2.1. EBSD

Maraging steels exhibit commendable strength and toughness, attributes achieved through age hardening, or ageing, of a ductile, low-carbon body-centred cubic (BCC) martensitic structure with relatively robust strength [16]. The inverse pole figure (IPF) maps obtained by EBSD for supplier 1 (Figure 18) reveal the grain structure along XY and Z sections, respectively, with a full BCC crystal structure. The IPF map in Figure 18a, observed along the XY section similar to Figure 14a, shows a crossed grain structure obtained by the crossed remelting paths imposed by the laser. The progressive remelting, layer by layer, leaves behind a characteristic broken columnar structure that promotes grain refinement with enhanced mechanical properties. The remelt pool features of Figure 14b are also visible in Figure 18b, corresponding to the Z section with the typical columnar grain growth parallel to the heat gradient during solidification. A refined grain structure is better perceived in the grain boundary maps displayed in Figure 14c,d, with an average grain size of 3.07 and 3.22 μm , respectively (grains touching the observation field limits were not considered). Sub grain boundaries, a 5–15° misorientation angle, accounting for nearly 20% of the total boundaries, is identified on both maps. A high entropy structure is a result of quick solidification and cooling processes, which will promote structure recrystallisation in the subsequent heating and cooling steps during the fusion of upper layers. Grain growth is very limited due to the quick nature of these steps, which results in a refined grain structure. Texture plots in Figure 14e,f suggest different crystallographic orientation preferences between section XY and section Z. The calculated orientation distribution peak for Z is approximately two-fold higher than for the XY section. However, the interpretation of texture based on these maps is somewhat limited since the area observed is relatively small. A larger observed area coupled with a higher-resolution image would be required for a more statistically significant texture analysis.

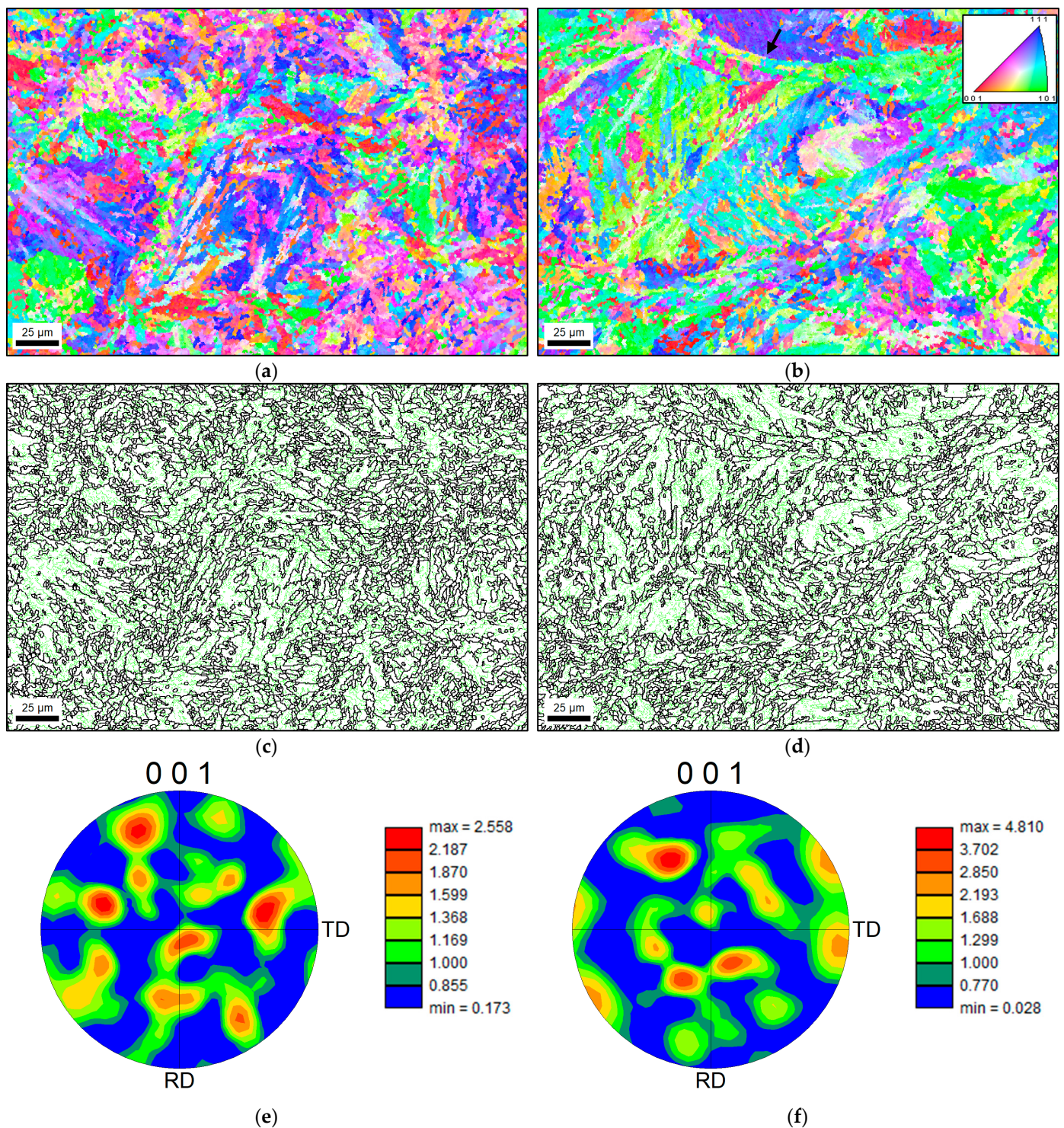


Figure 18. Inverse pole figure (IPF) was obtained by EBSD for the XY (a) and Z (b) sections. Remelting pool boundary (black arrow). Grain boundary map for the XY (c) and Z (d) sections. Green and black boundaries represent 5–15° and 5–180° angle ranges, respectively. Texture plots for the XY (e) and Z (f) sections.

3.2.2. Impact Testing

Charpy impact tests (Table 6) further highlight the crucial influence of both build orientation and heat treatment on the impact resistance of supplier 1's L-PBF maraging steel part. As-built specimens demonstrated a striking anisotropy: Z-oriented specimens exhibited significantly higher impact energy absorption (38.6 J) than XY-oriented specimens

(4.4 J). This aligns with the expected impact behaviour due to the layer-by-layer nature of the L-PBF process. While post-build ageing led to a marginal improvement in impact energy for XY specimens (4.9 J), it had minimal effect on the already higher toughness of Z-oriented specimens (36.5 J). These findings indicate that while heat treatment can offer some benefits, build orientation remains the dominant factor influencing impact resistance. This emphasises the importance of carefully considering both build parameters and potential post-processing treatments during the design and manufacturing stages to achieve the desired impact performance in L-PBF parts.

Table 6. Charpy impact test results for supplier 1, as-built and ageing, in building directions XY and Z.

Orientation	Build Orientation	Energy (J)
XY	XY	4.4 ± 0.4
	Z	38.6 ± 0.9
Z	Z	4.9 ± 0.5
	XY	37 ± 1

3.2.3. Heat Treatment Effects

Heat treatment dramatically altered the microstructure and mechanical properties of supplier 1's L-PBF maraging steel part. Age hardening, compared to the as-built condition (Figure 19), resulted in a substantial increase in hardness, particularly in the Z-direction which showed an increase of around 40% (from 371 ± 13 HV to 522 ± 23 HV in XY, and from 388 ± 17 HV to 566 ± 29 HV in Z) [61]. This improvement is attributed to the formation of intermetallic precipitates, which refine the microstructure and promote homogenous precipitate distribution. Microstructural analysis (Figure 20) confirms this transformation, revealing that both ageing (A) and solubilisation with ageing (SA) treatments eliminate the characteristic as-built cellular/columnar microstructure. This is replaced by a massive martensitic structure with very fine precipitates, explaining the increased hardness.

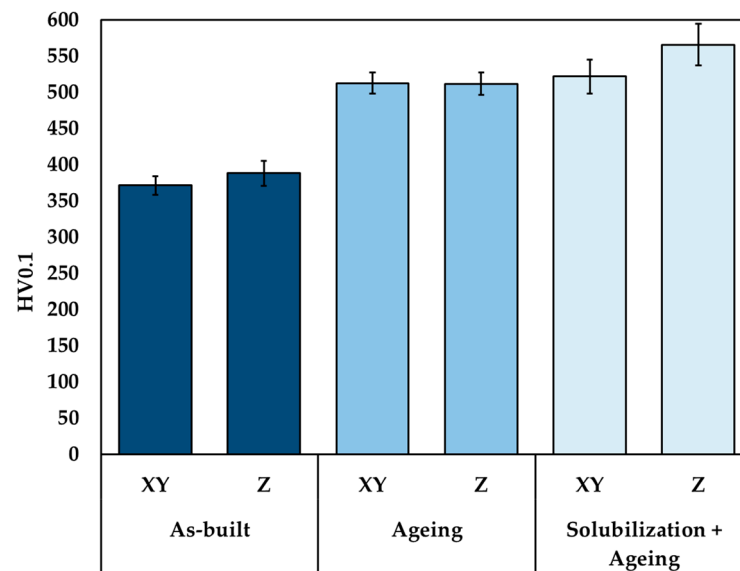


Figure 19. Hardness measurements obtained for supplier 1. Comparison between as-built, aged, and solubilised + aged conditions.

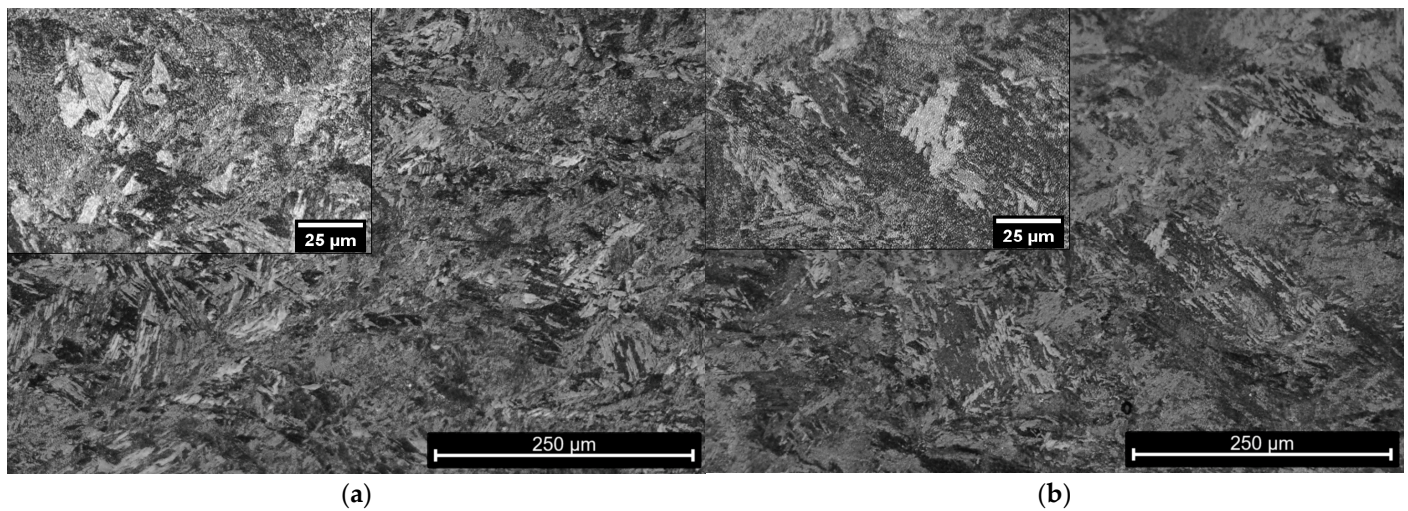


Figure 20. OM images from the Z section of the heat-treated specimens for supplier 1 ((a) SA, (b) A).

While hardness measurements suggest a slight advantage for solubilisation treatments, microstructural observations (Figure 20) reveal minimal differences between the A and SA conditions. This raises the possibility that the microstructural “history” induced by the L-PBF process itself may facilitate the formation of a refined microstructure during ageing, even without a separate solubilisation step. Further investigation is warranted to determine if the practical benefits of solubilisation outweigh the additional processing time and energy costs involved.

3.2.4. Tensile Testing

Tensile tests (Table 7) exposed anisotropy in the mechanical behaviour of supplier 1’s L-PBF maraging steel part. Z-oriented specimens (aligned with the build direction) demonstrated superior yield strength ($R_{p0.2} = 1066 \pm 52$ MPa), ultimate tensile strength ($R_m = 1178 \pm 16$ MPa), and elongation at fracture ($13 \pm 1\%$) compared to XY-oriented specimens. Conversely, XY specimens exhibited a higher modulus of elasticity ($E = 212 \pm 69$ GPa) than their Z-oriented counterparts ($E = 208 \pm 57$ GPa). This distinct variation in strength, ductility, and stiffness underscores the profound impact of build orientation on the mechanical properties of L-PBF-manufactured parts. Understanding and accounting for this anisotropy, driven by the process-induced microstructure, is essential when designing L-PBF parts to ensure they meet the specific performance demands of their intended applications.

Table 7. Tensile strength for supplier 1.

Orientation	$R_{p0.2}$ (MPa)	R_m	E (GPa)	Elongation (%)
XY	972 ± 53	1073 ± 13	212 ± 69	9 ± 1
Z	1066 ± 52	1178 ± 16	208 ± 57	13 ± 1

4. Conclusions

To fully realise the potential of AM for die manufacturing, this study undertakes a comprehensive benchmarking analysis of four L-PBF systems encompassing powder analysis, dimensional accuracy, surface finish, microstructure, and hardness. The main conclusions are as follows:

- Powders present variations in particle morphology and amount of oxide inclusions. It was also observed that the presence of particle clusters or elongated particles, in some cases, can potentially impact powder bed and melt pool behaviours.

- The observed variations in dimensional accuracy between suppliers underscore the profound sensitivity of L-PBF processes to parameter variations. These variations can significantly alter thermal gradients and shrinkage behaviour within the part.
- Suppliers 1 and 4 had the best surface finish. Process parameters and powder characteristics likely influence surface roughness.
- Suppliers 1, 3, and 4 exhibited typical L-PBF maraging steel microstructures with fine cellular and columnar grains growing perpendicular to the melt pool boundaries along the build direction, characteristic of rapid solidification conditions in L-PBF. The absence of clear cellular or dendritic features in supplier 2's microstructure suggests a different thermal history during processing, potentially involving extended laser exposure or a reheating strategy.
- Supplier 1 had, on average and considering both directions, the highest hardness, indicating that process parameter variations can significantly impact mechanical properties. The conclusions based on further characterisation of supplier 1 are as follows:
 - EBSD analysis showed a refined grain structure in XY and Z due to the rapid L-PBF process. Differences in crystallographic orientation between XY and Z sections suggest microstructural anisotropy.
 - Tensile test results demonstrated a significant anisotropy, with the Z section showing superior strength and ductility but lower stiffness.
 - Impact tests showed that the as-built Z section had superior toughness. Heat treatment had a minimal effect, emphasising this build orientation's dominance.
 - HT eliminates the characteristic as-built cellular/columnar microstructure. Age hardening transformed massive martensite into fine precipitates, resulting in a hardness increase from 371 to 522 HV and from 388 to 566 HV in XY and Z sections, respectively. Solubilisation before ageing offered a slight hardness gain, but its practical benefits need further investigation.
- The variability observed in this study reinforces the need for industry-wide standards in L-PBF, standardised process control methods and technical specifications for AM-produced components.

Author Contributions: Conceptualisation, J.M.C., E.W.S., R.F.S. and M.F.V.; formal analysis, J.M.C., E.W.S., R.F.S. and M.F.V.; investigation, J.M.C. and E.W.S.; methodology, J.M.C., E.W.S., R.F.S. and M.F.V.; project administration, J.M.C. and M.F.V.; supervision, M.F.V.; validation, J.M.C., E.W.S. and R.F.S.; visualisation preparation, J.M.C., E.W.S. and R.F.S.; writing, J.M.C., E.W.S. and R.F.S.; writing—review and editing, J.M.C., E.W.S., R.F.S. and M.F.V. All authors have read and agreed to the published version of the manuscript.

Funding: The authors gratefully acknowledge Hi-rEV—Recuperação do Setor de Componentes Automóveis (PRR-C644864375-00000002), which was partially funded by NextGeneration EU and the Plano de Recuperação e Resiliência (PRR), República Portuguesa.

Data Availability Statement: The data presented in this study are available on request from the corresponding author. The data are not publicly available due to privacy.

Acknowledgments: The authors express their gratitude to the former students and alums of the University of Porto's Faculty of Engineering Master's in Materials Engineering: Abel Oliveira, Bárbara Carvalho, Catarina Teixeira, Diogo Mota, Francisca Baptista, Henrique Moura, Maria Clara Luís, and João Torgal.

Conflicts of Interest: The authors declare no conflicts of interest.

References

1. Pereira, T.; Kennedy, J.V.; Potgieter, J. A comparison of traditional manufacturing vs. additive manufacturing, the best method for the job. In *Procedia Manufacturing*; Elsevier: Amsterdam, The Netherlands, 2019; Volume 30, pp. 11–18.
2. Nazir, A.; Gokcekaya, O.; Billah, K.M.M.; Ertugrul, O.; Jiang, J.; Sun, J.; Hussain, S. Multi-material additive manufacturing: A systematic review of design, properties, applications, challenges, and 3D printing of materials and cellular metamaterials. *Mater. Des.* **2023**, *226*, 111661. [[CrossRef](#)]

3. Ngo, T.D.; Kashani, A.; Imbalzano, G.; Nguyen, K.T.Q.; Hui, D. Additive manufacturing (3D printing): A review of materials, methods, applications and challenges. *Compos. Part B Eng.* **2018**, *143*, 172–196. [[CrossRef](#)]
4. Tofail, S.A.M.; Koumoulos, E.P.; Bandyopadhyay, A.; Bose, S.; O'Donoghue, L.; Charitidis, C. Additive manufacturing: Scientific and technological challenges, market uptake and opportunities. *Mater. Today* **2018**, *21*, 22–37. [[CrossRef](#)]
5. Jung, S.; Kara, L.B.; Nie, Z.; Simpson, T.W.; Whitefoot, K.S. Is Additive Manufacturing an Environmentally and Economically Preferred Alternative for Mass Production? *Environ. Sci. Technol.* **2023**, *57*, 6373–6386. [[CrossRef](#)]
6. Asnafi, N. Tool and Die Making, Surface Treatment, and Repair by Laser-based Additive Processes. *BHM Berg Hüttenmännische Monatshefte* **2021**, *166*, 225–236. [[CrossRef](#)]
7. Yoder, S.; Nandwana, P.; Paquit, V.; Kirka, M.; Scopel, A.; Dehoff, R.; Babu, S. Approach to qualification using E-PBF in-situ process monitoring in Ti-6Al-4V. *Addit. Manuf.* **2019**, *28*, 98–106. [[CrossRef](#)]
8. Hegab, H.; Khanna, N.; Monib, N.; Salem, A. Design for sustainable additive manufacturing: A review. *Sustain. Mater. Technol.* **2023**, *35*, e00576. [[CrossRef](#)]
9. Thomas, D. Costs, Benefits, and Adoption of Additive Manufacturing: A Supply Chain Perspective. *Int. J. Adv. Manuf. Technol.* **2016**, *85*, 1857–1876. [[CrossRef](#)]
10. DebRoy, T.; Wei, H.L.; Zuback, J.S.; Mukherjee, T.; Elmer, J.W.; Milewski, J.O.; Beese, A.M.; Wilson-Heid, A.D.; De, A.; Zhang, W. Additive manufacturing of metallic components—Process, structure and properties. *Prog. Mater. Sci.* **2018**, *92*, 112–224. [[CrossRef](#)]
11. Herderick, E. Additive Manufacturing of Metals: A Review. In Proceedings of the MS&T 2011: Proceedings from the Materials Science & Technology Conference, Columbus, OH, USA, 16–20 October 2011; pp. 1413–1425.
12. Vafadar, A.; Guzzomi, F.; Rassau, A.; Hayward, K. Advances in Metal Additive Manufacturing: A Review of Common Processes, Industrial Applications, and Current Challenges. *Appl. Sci.* **2021**, *11*, 1213. [[CrossRef](#)]
13. Costa, J.; Sequeiros, E.; Vieira, M.T.; Vieira, M. Additive Manufacturing: Material Extrusion of Metallic Parts. *U. Porto J. Eng.* **2021**, *7*, 53–69. [[CrossRef](#)]
14. Nunes, F.; Trindade, M.; Costa, J. Production and nTopology optimization of an additive manufactured support for smart glasses. *U. Porto J. Eng.* **2024**, *10*, 20–33. [[CrossRef](#)]
15. Moshiri, M.; Candeo, S.; Carmignato, S.; Mohanty, S.; Tosello, G. Benchmarking of Laser Powder Bed Fusion Machines. *J. Manuf. Mater. Process.* **2019**, *3*, 85. [[CrossRef](#)]
16. Yasa, E.; Kempen, K.; Kruth, J.P. Microstructure and mechanical properties of maraging steel 300 after selective laser melting. In Proceedings of the Solid Freeform Fabrication Symposium Proceedings, Austin, TX, USA, 9–11 August 2010.
17. Jäggle, E.; Sheng, Z.; Kürnsteiner, P.; Ocylok, S.; Weisheit, A.; Raabe, D. Comparison of Maraging Steel Micro- and Nanostructure Produced Conventionally and by Laser Additive Manufacturing. *Materials* **2016**, *10*, 8. [[CrossRef](#)]
18. Kempen, K.; Yasa, E.; Thijs, L.; Kruth, J.P.; Van Humbeeck, J. Microstructure and mechanical properties of Selective Laser Melted 18Ni-300 steel. In Proceedings of the Lasers in Manufacturing 2011: Proceedings of the Sixth International WIT Conference on Lasers in Manufacturing, Munich, Germany, 23–26 May 2011; Volume 12, pp. 255–263.
19. Thijs, L.; Van Humbeeck, J.; Kempen, K.; Yasa, E.; Kruth, J.P.; Rombouts, M. Investigation on the inclusions in maraging steel produced by Selective Laser Melting. In *Innovative Developments in Virtual and Physical Prototyping, Proceedings of the 5th International Conference on Advanced Research in Virtual and Rapid Prototyping, Leiria, Portugal, 28 September–1 October 2011*; CRC Press: Boca Raton, FL, USA, 2011.
20. Gao, W.; Zhang, Y.; Ramanujan, D.; Ramani, K.; Chen, Y.; Williams, C.B.; Wang, C.C.L.; Shin, Y.C.; Zhang, S.; Zavattieri, P.D. The status, challenges, and future of additive manufacturing in engineering. *Comput. Aided Des.* **2015**, *69*, 65–89. [[CrossRef](#)]
21. Garcia-Dominguez, A.; Claver, J.; Camacho, A.M.; Sebastian, M.A. Analysis of General and Specific Standardization Developments in Additive Manufacturing from a Materials and Technological Approach. *IEEE Access* **2020**, *8*, 125056–125075. [[CrossRef](#)]
22. Haghdadadi, N.; Laleh, M.; Moyle, M.; Primig, S. Additive manufacturing of steels: A review of achievements and challenges. *J. Mater. Sci.* **2021**, *56*, 64–107. [[CrossRef](#)]
23. Chowdhury, S.; Yadaiah, N.; Prakash, C.; Ramakrishna, S.; Dixit, S.; Gupta, L.R.; Buddhi, D. Laser powder bed fusion: A state-of-the-art review of the technology, materials, properties & defects, and numerical modelling. *J. Mater. Res. Technol.* **2022**, *20*, 2109–2172.
24. Dejene, N.D.; Lemu, H.G. Current Status and Challenges of Powder Bed Fusion-Based Metal Additive Manufacturing: Literature Review. *Metals* **2023**, *13*, 424. [[CrossRef](#)]
25. Gruber, S.; Grunert, C.; Riede, M.; López, E.; Marquardt, A.; Brueckner, F.; Leyens, C. Comparison of dimensional accuracy and tolerances of powder bed based and nozzle based additive manufacturing processes. *J. Laser Appl.* **2020**, *32*, 032016. [[CrossRef](#)]
26. Ameta, G.; Lipman, R.; Moylan, S.; Witherell, P. Investigating the Role of Geometric Dimensioning and Tolerancing in Additive Manufacturing. *J. Mech. Des.* **2015**, *137*, 111401. [[CrossRef](#)]
27. Mendricky, R.; Fris, D. Analysis of the Accuracy and the Surface Roughness of FDM/FFF Technology and Optimisation of Process Parameters. *Teh. Vjesn. Tech. Gaz.* **2020**, *27*, 1166–1173.
28. Thompson, S.M.; Bian, L.; Shamsaei, N.; Yadollahi, A. An overview of Direct Laser Deposition for additive manufacturing; Part I: Transport phenomena, modeling and diagnostics. *Addit. Manuf.* **2015**, *8*, 36–62. [[CrossRef](#)]
29. Frazier, W.E. Metal Additive Manufacturing: A Review. *J. Mater. Eng. Perform.* **2014**, *23*, 1917–1928. [[CrossRef](#)]
30. Chen, H.; Sun, Y.; Yuan, W.; Pang, S.; Yan, W.; Shi, Y. A Review on Discrete Element Method Simulation in Laser Powder Bed Fusion Additive Manufacturing. *Chin. J. Mech. Eng. Addit. Manuf. Front.* **2022**, *1*, 100017. [[CrossRef](#)]

31. Javidi, M.J.; Hosseini, S.; Khodabakhshi, F.; Mohammadi, M.; Orovciak, L.; Trembošová, V.N.; Nagy, Š.; Nosko, M. Laser powder bed fusion of 316L stainless steel/ Al_2O_3 nanocomposites: Taguchi analysis and material characterization. *Opt. Laser Technol.* **2023**, *158*, 108883. [[CrossRef](#)]
32. Jimenez Abarca, M.; Darabi, R.; de Sa, J.C.; Parente, M.; Reis, A. Multi-scale modeling for prediction of residual stress and distortion in Ti–6Al–4V semi-circular thin-walled parts additively manufactured by laser powder bed fusion (LPBF). *Thin-Walled Struct.* **2023**, *182*, 110151. [[CrossRef](#)]
33. Chua, C.K.; Wong, C.H.; Yeong, W.Y. *Chapter Eight—Benchmarking for Additive Manufacturing, in Standards, Quality Control, and Measurement Sciences in 3D Printing and Additive Manufacturing*; Chua, C.K., Wong, C.H., Yeong, W.Y., Eds.; Academic Press: Cambridge, MA, USA, 2017; pp. 181–212.
34. Montero, J.; Weber, S.; Petroll, C.; Brenner, S.; Bleckmann, M.; Paetzold, K.; Nedeljkovic-Groha, V. Geometrical Benchmarking of Laser Powder Bed Fusion Systems Based on Designer Needs. *Proc. Des. Soc.* **2021**, *1*, 1657–1666. [[CrossRef](#)]
35. Król, M.; Snopiński, P.; Hajnyš, J.; Pagáč, M.; Łukowiec, D. Selective Laser Melting of 18Ni-300 Maraging Steel. *Materials* **2020**, *13*, 4268. [[CrossRef](#)]
36. ISO 4287:1997; Geometrical Product Specifications (GPS)—Surface Texture: Profile Method—Terms, Definitions and Surface Texture Parameters. International Organization for Standardization: Geneva, Switzerland, 1997.
37. ISO 6507-1:2005; Metallic Materials—Vickers Hardness Test—Part 1: Test Method. International Organization for Standardization: Geneva, Switzerland, 2005.
38. Casalino, G.; Campanelli, S.L.; Contuzzi, N.; Ludovico, A.D. Experimental investigation and statistical optimisation of the selective laser melting process of a maraging steel. *Opt. Laser Technol.* **2015**, *65*, 151–158. [[CrossRef](#)]
39. Singh, R.; Davim, J.P. *Additive Manufacturing: Applications and Innovations*; CRC Press: Boca Raton, FL, USA, 2018.
40. ISO 6892-1:2012; Metallic Materials—Tensile Testing—Part 1: Method of Test at Room Temperature. International Organization for Standardization: Geneva, Switzerland, 2012.
41. ISO 148-1:2016; Metallic Materials—Charpy Pendulum Impact Test—Part 1: Test Method. International Organization for Standardization: Geneva, Switzerland, 2016.
42. Stegman, B.T.; Lopez, J.; Jarosinski, W.; Wang, H.; Zhang, X. The Influence of Powder Particle Size Distributions on Mechanical Properties of Alloy 718 by Laser Powder Bed Fusion. *Metals* **2023**, *13*, 1384. [[CrossRef](#)]
43. Anderson, I.E.; White, E.M.H.; Dehoff, R. Feedstock powder processing research needs for additive manufacturing development. *Curr. Opin. Solid State Mater. Sci.* **2018**, *22*, 8–15. [[CrossRef](#)]
44. Iams, A.D.; Keist, J.S.; Giannuzzi, L.A.; Palmer, T.A. The Evolution of Oxygen-Based Inclusions in an Additively Manufactured Super-Duplex Stainless Steel. *Metall. Mater. Trans. A* **2021**, *52*, 3401–3412. [[CrossRef](#)]
45. Deng, P.; Karadge, M.; Rebak, R.B.; Gupta, V.K.; Prorok, B.C.; Lou, X. The origin and formation of oxygen inclusions in austenitic stainless steels manufactured by laser powder bed fusion. *Addit. Manuf.* **2020**, *35*, 101334. [[CrossRef](#)]
46. Mata, M.; Pinto, M.; Costa, J. Topological Optimization of a Metal Extruded Doorhandle using nTopology. *U. Porto J. Eng.* **2023**, *9*, 42–54. [[CrossRef](#)]
47. Kuo, Y.H.; Cheng, C.-C.; Lin, Y.-S.; San, C.-H. Support structure design in additive manufacturing based on topology optimization. *Struct. Multidiscip. Optim.* **2018**, *57*, 183–195. [[CrossRef](#)]
48. Gibson, I.; Rosen, D.W.; Stucker, B. *Additive Manufacturing Technologies: Rapid Prototyping to Direct Digital Manufacturing*; Springer: New York, NY, USA, 2010.
49. Nunes, H.; Costa, J.M.; Viana, F.; Vieira, M.F. Additively Manufactured Ti-6Al-4V: Effects of Heat-Treatment. *Mater. Proc.* **2022**, *8*, 111. [[CrossRef](#)]
50. Sarafan, S.; Wanjara, P.; Gholipour, J.; Bernier, F.; Osman, M.; Sikan, F.; Molavi-Zarandi, M.; Soost, J.; Brochu, M. Evaluation of Maraging Steel Produced Using Hybrid Additive/Subtractive Manufacturing. *J. Manuf. Mater. Process.* **2021**, *5*, 107. [[CrossRef](#)]
51. Sendino, S.; Martinez, S.; Lartategui, F.; Gardon, M.; Lamikiz, A.; Gonzalez, J.J. Effect of powder particle size distribution on the surface finish of components manufactured by laser powder bed fusion. *Int. J. Adv. Manuf. Technol.* **2023**, *124*, 789–799. [[CrossRef](#)]
52. Rao, B.S.; Rao, T.B. Effect of Process Parameters on Powder Bed Fusion Maraging Steel 300: A Review. *Lasers Manuf. Mater. Process.* **2022**, *9*, 338–375. [[CrossRef](#)]
53. Thijs, L.; Kempen, K.; Kruth, J.-P.; Van Humbeeck, J. Fine-structured aluminium products with controllable texture by selective laser melting of pre-alloyed AlSi10Mg powder. *Acta Mater.* **2013**, *61*, 1809–1819. [[CrossRef](#)]
54. Tan, C.L.; Zhou, K.; Ma, W.; Zhang, P.; Liu, M.; Kuang, T. Microstructural evolution, nanoprecipitation behavior and mechanical properties of selective laser melted high-performance grade 300 maraging steel. *Mater. Des.* **2017**, *134*, 23–34. [[CrossRef](#)]
55. Narasimharaju, S.R.; Zeng, W.; See, T.L.; Zhu, Z.; Scott, P.; Jiang, X.; Lou, S. A comprehensive review on laser powder bed fusion of steels: Processing, microstructure, defects and control methods, mechanical properties, current challenges and future trends. *J. Manuf. Process.* **2022**, *75*, 375–414. [[CrossRef](#)]
56. Santana, A.; Eres-Castellanos, A.; Jimenez, J.A.; Rementeria, R.; Capdevila, C.; Caballero, F.G. Effect of layer thickness and laser emission mode on the microstructure of an additive manufactured maraging steel. *J. Mater. Res. Technol.* **2023**, *25*, 6898–6912. [[CrossRef](#)]
57. Sanjari, M.; Mahmoudiniya, M.; Pirgazi, H.; Tamimi, S.; Ghoncheh, M.H.; Shahriari, A.; Hadadzadeh, A.; Amirkhiz, B.S.; Purdy, M.; de Araujo, E.G.; et al. Microstructure, texture, and anisotropic mechanical behavior of selective laser melted maraging stainless steels. *Mater. Charact.* **2022**, *192*, 112185. [[CrossRef](#)]

58. Campanelli, S.L.; Contuzzi, N.; Posa, P.; Angelastro, A. Study of the aging treatment on selective laser melted maraging 300 steel. *Mater. Res. Express* **2019**, *6*, 066580. [[CrossRef](#)]
59. Takata, N.; Nishida, R.; Suzuki, A.; Kobashi, M.; Kato, M. Crystallographic Features of Microstructure in Maraging Steel Fabricated by Selective Laser Melting. *Metals* **2018**, *8*, 440. [[CrossRef](#)]
60. Tekin, T.; Ischia, G.; Naclerio, F.; Ipek, R.; Molinari, A. Effect of a direct aging heat treatment on the microstructure and the tensile properties of a 18Ni-300 maraging steel produced by Laser Powder Bed Fusion. *Mater. Sci. Eng. A* **2023**, *872*, 144921. [[CrossRef](#)]
61. Mutua, J.; Nakata, S.; Onda, T.; Chen, Z.-C. Optimization of selective laser melting parameters and influence of post heat treatment on microstructure and mechanical properties of maraging steel. *Mater. Des.* **2018**, *139*, 486–497. [[CrossRef](#)]

Disclaimer/Publisher’s Note: The statements, opinions and data contained in all publications are solely those of the individual author(s) and contributor(s) and not of MDPI and/or the editor(s). MDPI and/or the editor(s) disclaim responsibility for any injury to people or property resulting from any ideas, methods, instructions or products referred to in the content.